TOPICAL REVIEW

Single ion induced surface nanostructures: a comparison between slow highly charged and swift heavy ions

Friedrich Aumayr[1,6]**, Stefan Facsko**[2]**, Ayman S El-Said**[1,2,3]**, Christina Trautmann**[4] **and Marika Schleberger**[5]

[1] Institute of Applied Physics, TU Wien, 1040 Vienna, Austria
[2] Institut für Ionenstrahlphysik und Materialforschung, Helmholtz-Zentrum Dresden-Rossendorf, 01328 Dresden, Germany
[3] Physics Department, Faculty of Science, Mansoura University, 35516 Mansoura, Egypt
[4] GSI Helmholtz Centre for Heavy Ion Research, 64291 Darmstadt, Germany
[5] Fakultät für Physik, Universität Duisburg-Essen, 47048 Duisburg, Germany

E-mail: aumayr@iap.tuwien.ac.at

Abstract

This topical review focuses on recent advances in the understanding of the formation of surface nanostructures, an intriguing phenomenon in ion–surface interaction due to the impact of individual ions. In many solid targets, swift heavy ions produce narrow cylindrical tracks accompanied by the formation of a surface nanostructure. More recently, a similar nanometric surface effect has been revealed for the impact of individual, very slow but highly charged ions. While swift ions transfer their large kinetic energy to the target via ionization and electronic excitation processes (electronic stopping), slow highly charged ions produce surface structures due to potential energy deposited at the top surface layers. Despite the differences in primary excitation, the similarity between the nanostructures is striking and strongly points to a common mechanism related to the energy transfer from the electronic to the lattice system of the target. A comparison of surface structures induced by swift heavy ions and slow highly charged ions provides a valuable insight to better understand the formation mechanisms.

(Some figures in this article are in colour only in the electronic version)

Contents

[6] Address for correspondence: Institute of Applied Physics, TU Wien—Vienna University of Technology, Wiedner Hauptstraße 8-10/E134, 1040 Vienna, Austria.

1. Introduction

This topical review compiles common phenomena of nanometric surface modifications induced by slow highly charged ions (HCI) and swift heavy ions (SHI). Before going into detail, it is important to understand the specific properties of each of these beams.

Slow highly charged ions are characterized by their low velocity and high potential energy, which is stored due to the removal (ionization) of many or even all electrons from a neutral atom. The potential energy of HCI is given by the sum of all binding energies of the missing electrons and can reach values of several tens up to hundreds of keV (figure 1(b)) [1]. The term slow usually refers to impact velocities smaller than one in atomic units corresponding to projectile velocities of 2.18×10^6 m s^{-1} or specific energies below 25 keV/amu. At such low impact velocity, electronic transitions between the highly charged projectile and a solid surface are generally much faster than significant changes of the projectile–surface distance. With the currently available HCI sources such as electron beam ion traps (EBITs) or electron cyclotron resonance ion sources (ECRISs) it is possible to produce HCI beams, where the potential energy of the HCI exceeds their kinetic energy by far or at least dominates the interaction processes in a surface near region.

Swift heavy ions are characterized by the fact that slowing down in matter occurs predominately by electronic excitation and ionization processes (electronic stopping). As shown in figure 1(a), this criterion is fulfilled for kinetic energies around the maximum of the energy loss curve (several tens of MeV) and above. Elastic collisions (nuclear stopping) with the target atoms play a minor role and come into play only at the end of the trajectory for energies of a few hundred keV and below. The term 'heavy' is less well defined but excludes protons, alphas, and other low-mass particles of limited energy loss values. SHI are typically produced in large scale facilities where initially low charged ions are accelerated up to energies of MeV to GeV, corresponding to a few per cent of the velocity of light and above. The charge state of SHI depends on the projectile velocity, because in a target the ions strip off all those electrons whose Bohr velocity is

slower than the beam velocity. This typically leads to a charge distribution around the equilibrium charge state. In many large accelerator facilities, stripper foils are used at low ion velocity and a projectile of specific charge is selected for the final accelerating stage. This yields projectiles of fixed charge state which is lower than the equilibrium charge state (e.g. the UNILAC of GSI provides 2.25 GeV U^{28+} ions whereas the equilibrium charge state at this energy is $\langle q \rangle \sim 59$). When impinging the target, the projectiles strip off electrons within the first layers of the solid.

It has been known for decades that the irradiation of solid targets with SHI can lead to permanent structural modifications in the bulk and at the surface (see e.g. [4–10] and references therein). Each individual projectile induces a long, straight nanometric track consisting of amorphous or otherwise modified material. At the impact site of the ion usually a hillock- or crater-type nanostructure is created. The formation of tracks and surface nanostructures occurs predominantly in insulators (e.g. polymers, oxides, ionic crystals) and is linked to a critical (electronic) energy loss dE/dx (see figure 1(a)) of the projectiles.

Electronic stopping of swift heavy ions is well known to induce intense electronic excitations within a confined volume around the ion trajectory and is the major cause for the formation of tracks and surface structures [11]. The exact mechanism of how this excitation energy is transferred to the lattice atoms is still under discussion and obviously depends on the type of material. Several mechanisms have been proposed. In the Coulomb explosion model (e.g. [12]) the passing projectile ionizes atoms of the target. Subsequently, the positively charged lattice atoms repel each other producing a shock wave. In the thermal spike model (e.g. [13]), the ion energy is first transferred to the electron subsystem where it is dissipated into a larger volume. In a second step (the electronic excitation and atomic motion occur on completely different time scales) the energy is transferred to the lattice atoms where it contributes to local heating. Depending on the material, the process is sufficiently efficient to locally increase the temperature above melting (thermal spike). A rapid temperature drop finally quenches the molten phase producing the track and a surface hillock.
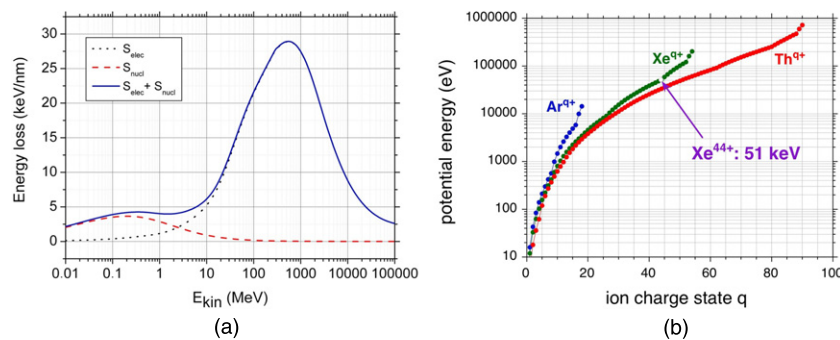

Figure 1. (a) Energy losses due to nuclear and electronic stopping as a function of kinetic energy in MeV as calculated with the SRIM code [2, 3] for the irradiation of SrTiO$_3$ with Xe ions. (b) Total potential energy of highly charged Ar^{q+}, Xe^{q+} and Th^{q+} ions versus charge state q. Xe^{44+}, for example, has a potential energy of about 51 keV.

Recent investigations illustrated that individual slow highly charged ions produce similar surface modifications. In analogy to the dE/dx threshold of SHI, the formation of HCI induced surface structures also requires that the potential energy exceeds a critical value (see e.g. [14–17] and references therein). The potential energy of slow HCI can become comparable to or even considerably higher than the kinetic energy, resulting in a significant contribution to electron emission and sputtering (potential electron emission [18–20], potential sputtering [1, 21–27]). Under ion irradiation, these surface phenomena are usually dominated by kinetic energy effects (kinetic electron emission [28–33], kinetic sputtering [11, 34]). The kinetic energy of HCI can be extremely small, limiting their penetration into the target to a few atomic layers. The entire potential energy is deposited into a nanometer size volume close to the surface [1, 20, 35–37]. Radiation defects in deeper layers are thus avoided, making HCI beams a gentle tool for surface nanostructuring, cleaning, and modifications. The use of slow highly charged ions instead of swift heavy ions might therefore also be of interest for nanostructuring of surfaces and related applications.

The primary electronic excitation processes by HCI occur on a femtosecond time scale and are followed by relaxation processes in the target lattice. At present, unfortunately no experimental techniques are available to study the kinetics of all different stages of the formation of the surface nanostructures. However, the similarity between surface structures induced by SHI and slow HCI impacts is striking and strongly points to common mechanisms at work. In the following, we present experimental evidence with special emphasis on slow HCI induced nanostructures (section 2). Effects due to SHI impacts have already been described in the literature [38–43] and are mainly shown for comparison purposes. The similarities and differences between slow HCI and SHI impacts are compiled in section 3, in particular the circumstances and conditions under which nano-sized features on particular surfaces can be produced. Finally, we attempt to present a possible common scenario for the formation of SHI and HCI induced surface structures (section 4).

2. Phenomenological comparison between SHI and HCI generated nanostructures

Most experimental results on beam induced surface structures available to date were obtained by means of scanning probe microscopy. These imaging techniques offer the unique possibility to identify and characterize localized surface modifications in extreme cases even down to the subatomic scale [44]. Before comparing experimental SHI and HCI data, we briefly discuss the advantages and limitations due to a variety of (non-instrumental) artifacts limiting the resolution as well as the meaningfulness of the method. For conductive samples, scanning tunneling microscopy (STM) is known to provide convoluted information on the topography and electronic density of states (DOS) at the Fermi edge [45]. Without the knowledge of the exact geometry of the tip and its electronic band structure, it is in principle impossible to deduce the correct topography of a nanostructure by STM alone. Additional problems such as elastic deformations or multiple tips [46] may further complicate the interpretation of STM images. The restriction of STM to electrically conductive samples is overcome by using atomic force microscopy (AFM). The imaging is based on a non-monotonic behavior of the force–distance curve and requires a more complex feedback loop. A variety of operating principles (contact, tapping, non-contact in ultra-high vacuum) yields different topographic information [47]. The imaging resolution provided by AFM is in general less than for STM. Sometimes AFM images give only the illusion of atomic resolution, as for example in the case of highly oriented pyrolytic graphite (HOPG), where flakes from the sample easily attach to the tip and results in a perfect registry between this tip-flake and the HOPG sample (atomic lattice imaging) [48]. Therefore, the existence of single atomic defects in an image may serve as an unambiguous criterion for true atomic resolution, see e.g. [49].

When analyzing AFM images, even if recorded without atomic resolution, convolution effects have to be considered when the tip and the surface features to be imaged are of similar size. Methods for tip calibration and deconvolution procedures have been proposed [50] and applied [51]. However, most diameters reported for ion induced hillocks were not corrected and thus have to be treated with care. In contrast, hillock height data are more reliable as the resolution in the z-direction even of air-operated AFMs is in general on the sub-Å scale and is not hampered by the tip shape (apart from multiple tips). For surface craters quite the opposite is true. Here the AFM tip size affects the depth rather than the diameter. Electrostatic interactions between the tip and the sample give rise to an additional force, which may vary locally and must be compensated if true heights are to be measured [52]. This technique requires an extra feedback loop and is therefore not always applied.

In the following, the experimental results (both for HCI and SHI) are summarized for various target materials including different halides, oxides, graphite and polymers. The overview is limited to low fluence experiments with modifications due to individual ion impacts. Furthermore, we will discuss only data from surface-related experiments and/or studies determining threshold values. For the sake of convenience the kinetic energies of all SHI are converted to electronic stopping powers. When comparing the results from different irradiation experiments, special attention should be paid to the charge state of the SHI used because it directly determines the energy loss [53]. Non-equilibrium charge states may have smaller stopping powers to those assumed in standard codes (e.g. SRIM). In some experiments, a foil mounted in front of the sample adjusts the beam to the equilibrium charge state, but then the ions have a charge state distribution [54].

2.1. Halides

2.1.1. Potassium bromide KBr. The interaction of slow HCI with the surface of KBr has been well investigated [16, 55].
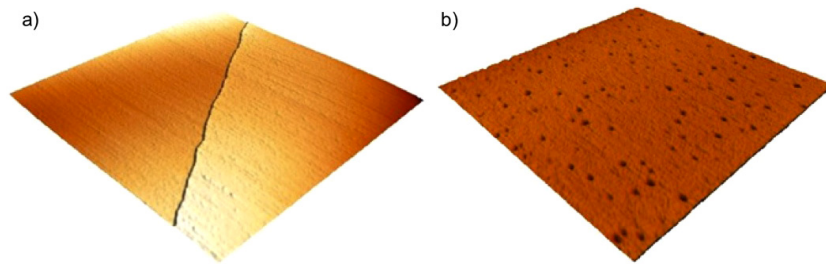
Figure 2. Surface images of KBr(100) recorded by contact AFM in ultra-high vacuum (UHV): (a) flat surface after cleavage in air with a monatomic step along the diagonal, (b) surface craters (dark spots) after irradiation with Xe^{25+} ions at a kinetic energy of 40 keV. Ion impacts are visible as nano-sized pit structures with monatomic depth of 0.4 nm. Image sizes are 1 μm × 1 μm [16].

KBr can be cleaved along the (100) planes exhibiting large defect-free terraces occasionally separated by monatomic steps (figure 2(a)). After irradiation with Xe^{25+} at 40 keV kinetic energy, pit-like structures are observed (figure 2(b)). These nano-pits are depressions of one atomic layer depth only. The huge loss of material is ascribed to pronounced sputtering by each incoming ion. The contact AFM images were recorded using a variable temperature AFM/STM from Omicron operated under ultra-high vacuum conditions.

The diameter and the depth of the pit structures were analyzed for a series of AFM images. The number of craters on a 1 μm × 1 μm area is 70–80, which is in good agreement with the applied fluence (8×10^9 cm^{-2}), indicating that for the given beam conditions every HCI creates a crater. Noticeably, the depth of the pits is 0.4 nm, corresponding to only one atomic distance in the (100) direction. None of the pits were deeper than one monolayer. The average diameter of the nano-pits is determined to 17 nm giving a pit volume of around 90 nm^3. To produce such a crater, a huge sputter yield of 1800 atoms/ion has to be assumed, while the sputter yield expected from the kinetic energy of the ions is only 5 atoms/ion [56, 57]. Potential sputtering, i.e. sputtering due to the potential energy of the HCI [1, 21, 24, 25] is known to occur for slow HCI impact on alkali halide surfaces and is therefore the most probable mechanism for the crater formation.

Irradiations were performed for different kinetic energies and charge states of the Xe ions, thus varying the potential energy from 31 eV (Xe^{2+}) to 23 keV (Xe^{34+}). The result of these systematic investigations can be presented as a 'phase diagram' for the formation of pit structures (figure 3). For a fixed kinetic impact energy, a threshold in the potential energy has to be surpassed (shaded area in figure 3). The position of the threshold strongly depends on the kinetic energy. With increasing kinetic energy the threshold shifts to lower potential energy. Above the threshold the size of the pits increases linearly with the potential energy [55] (see figure 4).

In the case of SHI irradiation, KBr single crystals were investigated with respect to their optical properties [58, 59]. The irradiations were performed with stopping powers between 0.5 and 13 keV nm^{-1} and point defects produced by the self-trapped exciton (STE) mechanism were identified. At that time, neither track dimensions nor systematic surface investigations were performed. SHI irradiation experiments of cleaved KBr(100) samples at stopping powers of
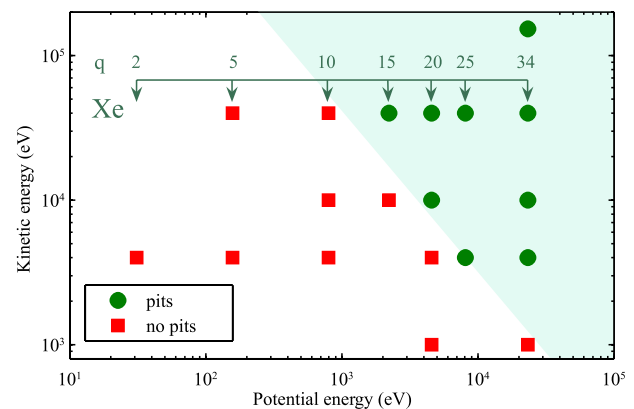

Figure 3. Phase diagram for the formation of pit structures on KBr(100) surfaces by the impact of highly charged Xe ions. Irradiations with and without pit structures are marked by green circles and red squares, respectively. For pit creation, the kinetic as well as the potential energy of the ions must surpass a critical value (gray area). The diagram uses data from [55].
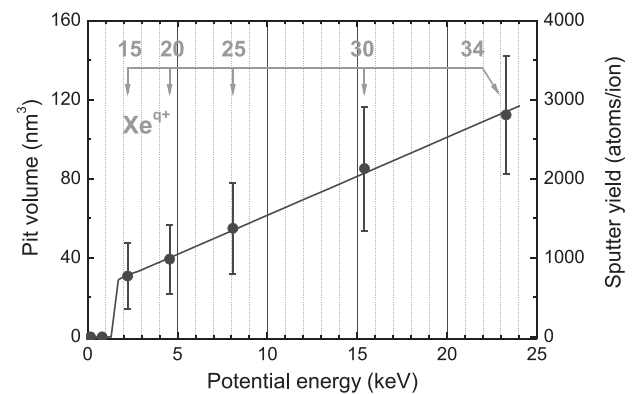

Figure 4. Pit volume (left axis) and corresponding sputter yield (right axis) as a function of the potential energy of the Xe^{q+} ions. The kinetic energy of the ions was 40 keV. The corresponding charge states are given on the upper scale (data from [55]).

10 keV nm^{-1} yielded no ion induced features detectable by tapping mode AFM under ambient conditions [60].

2.1.2. Calcium fluoride CaF$_2$. For CaF$_2$ a much larger data set from many different irradiations is available. Single fluorite crystals can easily be cleaved along the (111) planes
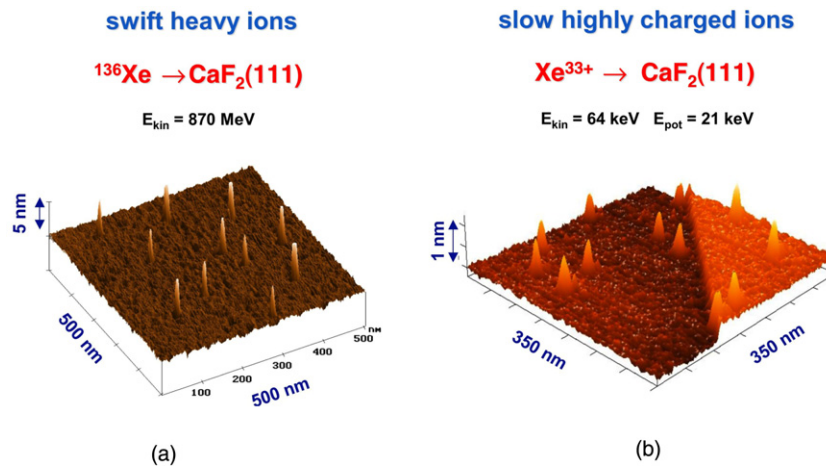
Figure 5. Topographic contact mode AFM images of $CaF_2(111)$ surfaces after irradiation with (a) 870 MeV Xe ions of 5×10^9 cm^{-2} (reproduced with permission from [51]. Copyright 2005 Elsevier) and (b) 64 keV Xe^{33+} ions showing hillock-like nanostructures protruding from the surface [15]). While the diameter of the hillocks is comparable, the hillock height is considerably larger for swift heavy ion impacts (note the different axis units of the images).
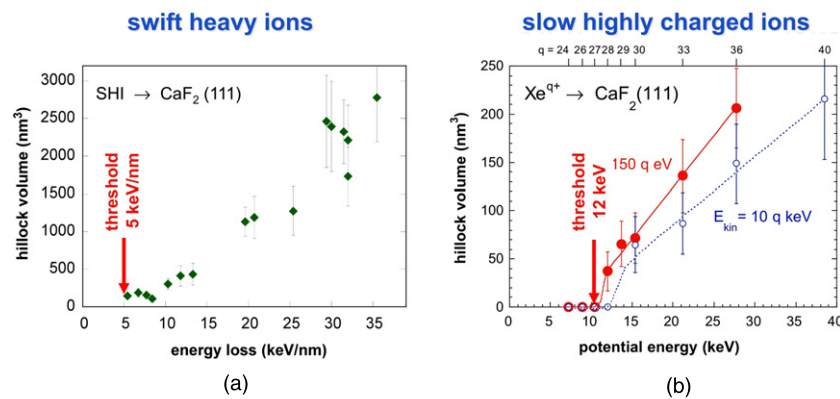

Figure 6. Hillocks formed on the surface of $CaF_2(111)$ single crystals: (a) mean hillock volume as a function of electronic energy loss of SHI (data from [66]). (b) Mean hillock volume as a function of potential energy of highly charged Xe^{q+} ions (data from [15, 62]). The threshold(s) for nano-hillock formation are indicated.

resulting in atomically flat fluorine-terminated surfaces. After irradiation with SHI, samples have been reported to remain stable in atmosphere at room temperature for several years [47]. In contrast to the pit formation in KBr crystals, the irradiation of $CaF_2(111)$ crystals with SHI as well as with slow HCI results in nano-sized hillocks (see figure 5). The AFM images show the surface topography of irradiated surfaces recorded in the contact mode. The diameter of SHI as well as HCI induced hillocks is about 20–40 nm, while the hillock height is only a few nanometers (~0.5–2 nm for HCI and up to ~15 nm for SHI). The height of the hillocks shown in figure 5 seems exaggerated due to the small z-axis units.

The number of the hillocks always corresponded with the applied ion fluence, indicating that every single ion impact produces one nano-hillock. Hillock formation by SHI was studied in detail for a large number of different light and heavy ions [51]. For slow HCI, nano-sized protrusions on CaF_2 were first reported for Xe^{44+} ions of 2 keV/amu kinetic energy [61], and later complemented by more systematic experiments using Ar and Xe ions with charge states ranging

from 11 to 48 [62]. The dependence on kinetic energy was investigated by decelerating HCI to kinetic energies as low as 150 eV $\times q$ [15].

Figure 6 shows the evolution of the hillock dimensions as a function of the respective beam parameter, i.e. electronic energy loss (SHI) and potential energy (HCI). If the diameter and height is measured, the volume of the hillocks can be determined by calculating the volume of a spherical cap. For HCI of a given kinetic energy, the hillock volume depends strongly on the projectile's potential energy and shows a threshold around 12–14 keV (see figure 6(b)) [15, 62, 63]. Below this potential energy, no hillocks were found regardless of the projectile ion species (Xe^{q+} or Ar^{q+}). Above the threshold the hillock volume increases with the charge state (figure 6(b)) [15, 62]. The hillock size, however, does not depend significantly on the kinetic energy for a given charge state [15]. For HCI, the potential energy is the decisive parameter for hillock formation. Similar to figure 3, in figure 7 the appearance or absence of HCI induced hillocks is shown for various potential and kinetic energy
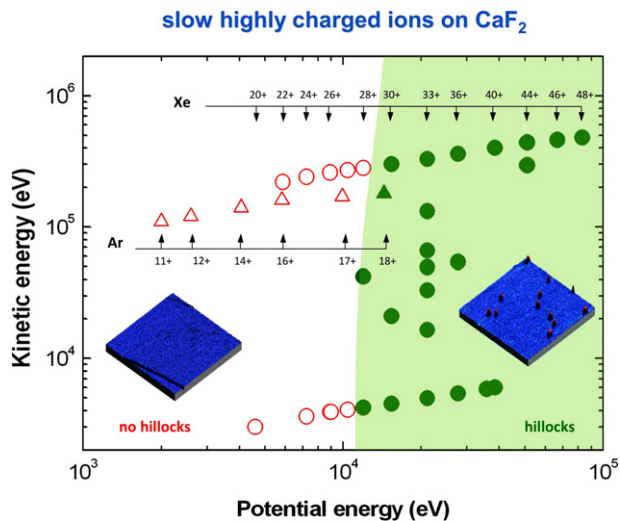
Figure 7. Hillock formation on CaF$_2$(111) irradiated with highly charged Xe (circles) and Ar (triangles) ions. For specific potential and kinetic energy combinations, the surface is flat and without hillocks (open symbols). Above about 12 keV potential energy hillocks (full symbols) are observed (green shaded area) almost independent of the kinetic projectile energy. The diagram uses data from [15, 61, 62].

combinations [16]. The threshold for hillock formation runs almost vertically through the plot, underlining the importance of the potential energy. This boundary is slightly tilted to the right at higher kinetic energies, which tells us that faster ions seem to require higher potential energies to induce hillocks. This counter-intuitive behavior suggests that additional kinetic energy provided to the system does not contribute significantly to hillock formation and is canceled out or even dominated by negative effects. With increasing potential energy, both the basal diameter and the height of the hillocks increase. For very large potential energies, a second threshold seems to appear (not indicated in figure 7) which is characterized by a further steep increase of the hillock size at around 50 keV (Xe^{44+}) [62].

The strong ionic binding character of ionic crystals such as CaF$_2$ or LiF prevents amorphization. Under SHI irradiation, damage is produced consisting of point defects as well as more complex defect aggregates (for an overview see [41]). Transmission electron microscopy of tracks of SHI and C$_{60}$ cluster ions shows intermittent faceted nanostructures aligned along the projectile trajectories. The faceted structures are attributed to anion voids equivalent to Ca colloids [64]. At the surface, the crystal is probably depleted of fluorine, resulting in Ca inclusions as detected by means of scanning probe microscopy applying the eddy current mode [65]. The first observation of SHI induced hillocks on CaF$_2$ was reported in 2002 [66]. According to a later more detailed study of Khalfaoui *et al* [47, 51], the threshold for hillock creation is $S_e = 5 \pm 0.8$ keV nm^{-1} [47, 51], in agreement with [66]. Above the threshold, the hillock height increases linearly with increasing energy loss, reaching a maximum value of 13 nm at 35 keV nm^{-1}. Typical reported diameters are $d \approx 20$ nm.

For CaF$_2$ it has explicitly been shown that the exact details of the hillock morphology depend strongly on the measuring mode (contact, tapping or dynamic) as well as on environmental conditions (e.g. humidity) due to the hygroscopic property of fluorite [47, 51, 67]. For a given sample, the apparent height of the SHI induced hillocks measured with different AFM modes varies between 4 and 9 nm; non-contact modes or measurements in vacuum lead typically to higher values. In addition to the formation of nanoscopic hillocks, other rather macroscopic surface phenomena are observed: at higher fluences SHI irradiated CaF$_2$ shows defect induced volume expansion (swelling) [68]. A direct correlation to hillock formation is not clear but swelling has a similar dE/dx threshold [51, 69]. Furthermore, SHI induce sputtering with huge yields compared to sputtering in the nuclear stopping regime. Depending on dE/dx up to several tens of thousands of atoms are released per incoming ion. Without the contribution of sputtering, the hillocks thus would be even larger.

2.1.3. Barium fluoride BaF$_2$. Motivated by the similarity to CaF$_2$, hillock formation was also investigated for the ionic crystal BaF$_2$ [70]. BaF$_2$(111) surfaces were irradiated with 4.5q keV highly charged Xe ions and subsequently inspected with contact AFM. Surprisingly, none of the surfaces irradiated with Xe^{q+} ($q = 24$–36) ions showed topographic changes. To reveal the damage produced by the HCI, chemical etching was performed using a 1 vol% solution of HNO$_3$ at room temperature without agitation. All samples were etched under identical conditions (i.e. concentration and etching time). The irradiation was performed through a rectangular copper grid, thus parts of the sample surface were masked. The observation of well-defined patterns is hence straightforward evidence of successful chemical etching of damage induced by HCI projectiles. Moreover, one can easily differentiate between features created due to ion irradiation and naturally present dislocations, which are also etchable. The AFM topographic image of a BaF$_2$ surface irradiated with Xe^{28+} ions after chemical etching shows three-faced symmetric pyramidal depressions for each ion impact (figure 8). This geometry originates from the (111) crystal lattice orientation of BaF$_2$. The volume of the etch pits (calculated assuming a three-faced symmetric pyramidal shape) shows a nearly linear increase with potential energy [70] (figure 9).

Very recently hillocks could be observed for impact of Xe^{33+} ions (figure 10), but this required deceleration to 165 keV [71]. Chemical etching under the same conditions as above dissolved all hillocks leading again to the well known etch pits of three-faced symmetric pyramidal depressions (see figure 10).

Surface hillocks produced with SHI were investigated in the electronic energy losses ranging from 8–38 keV nm^{-1} [42, 72]. The height was determined by contact mode AFM to be ~4 nm, while higher hillocks were found in tapping mode (figure 11). The applied fluence of 5×10^8 ions cm^{-2} corresponds well with the number of hillocks protruding from the rather rough surface (3–4 nm). While the height of the hillocks remains almost constant, their volume increases as a function of the energy loss of the ions [72]. Deduced from the
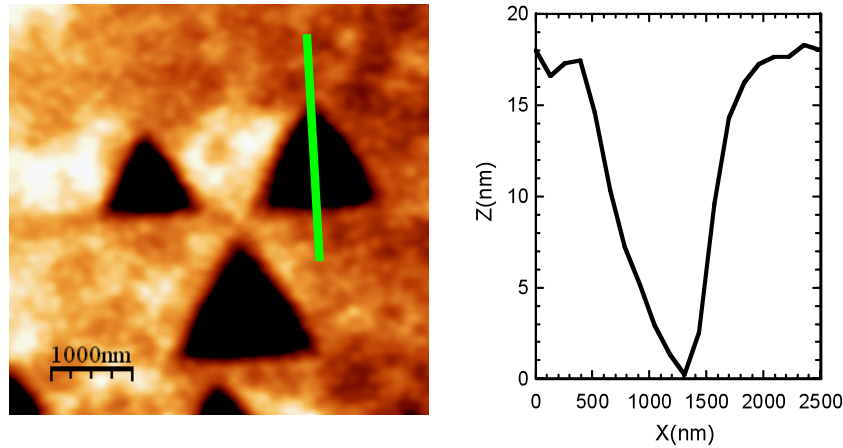
Figure 8. Topographic AFM image (left) of $BaF_2(111)$ irradiated with 126 keV Xe^{28+} ions and subsequent etching in HNO_3. Line profile across one of the etch pits (right) (from [70]).
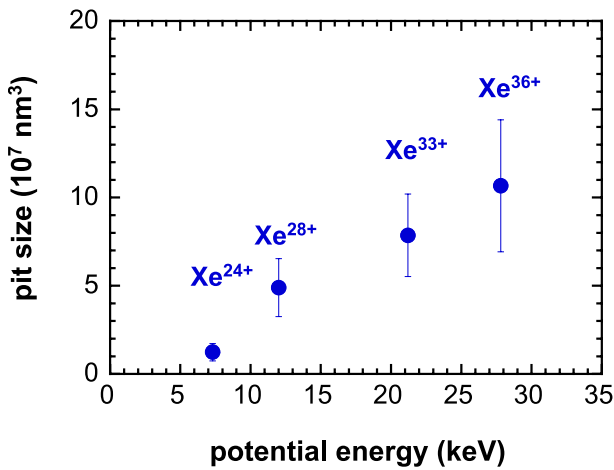

Figure 9. Mean volume (see text) of etch pits on $BaF_2(111)$ as a function of potential energy of $4.5 \times q$ keV Xe^{q+} ions (from [70]).

contact AFM data, the threshold for hillock creation in BaF_2 is around 3 keV nm^{-1} (figure 11).

2.1.4. Lithium fluoride LiF. Due to lack of sufficiently defect-free single crystals, which remain stable in air, existing results for LiF irradiated with HCI are only preliminary. LiF easily cleaves along one of the cubic planes and the surfaces irradiated with Xe^{q+} ions ($q \geq 28$) exhibit similar hillocks as in the case of CaF_2. Figure 12 shows hillocks created with 440 keV Xe^{44+} ions [73], however systematic studies for slow HCI impacts are still missing.

LiF is sensitive to almost any kind of ionizing radiation and has been studied extensively in the SHI community. As early as 1958 it was shown that chemical etching of SHI irradiated LiF crystals yields pyramid-shaped etch pits [74]. It is one of the few materials where a molecular dynamics (MD) simulation actually predicts the creation of hillocks on the surface [75].

As in CaF_2, tracks in LiF are not amorphous but consist of single defects and defect clusters. A series of complementing experiments revealed a complex track substructure consisting of a small core (1–2 nm in diameter) surrounded by a defect-rich halo with a radius of up to 30–50 nm [76]. Details depend on the electronic energy loss. The creation of the track core requires a threshold of $dE/dx \sim 10$ keV nm^{-1}, and is correlated with the formation of complex defect clusters [77] and possibly non-percolating metallic Li colloids [76]. Irradiated LiF also exhibits pronounced macroscopic swelling effects which appear above an energy loss threshold of 4.2 keV nm^{-1} [78].

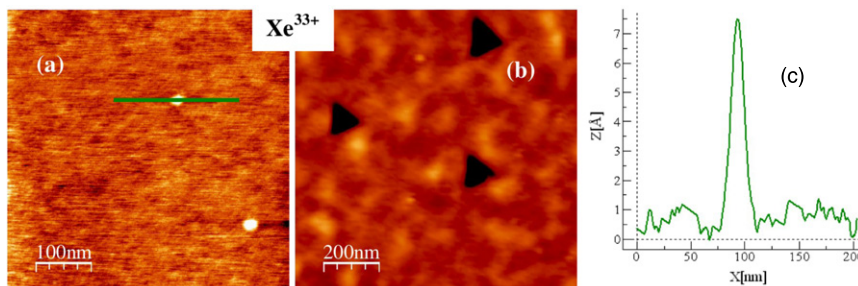**Figure 10.** AFM images of BaF_2 single crystal bombarded by 165 keV Xe^{33+} before (a) and after (b) chemical etching. (c) shows the height profile along one of the hillocks in (a). Reproduced with permission from [71]. Copyright 2001 Elsevier.
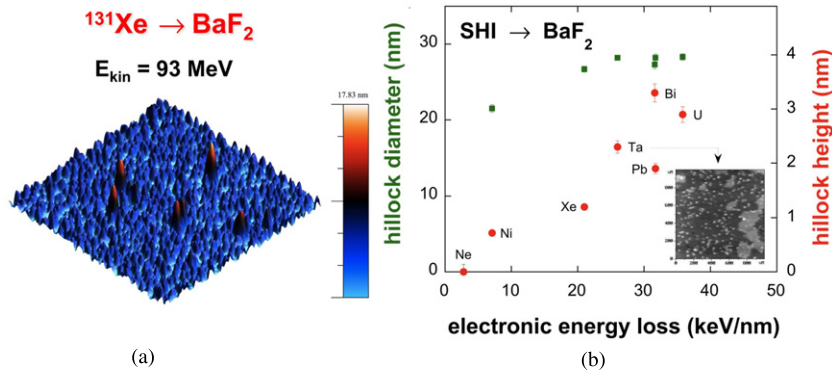
Figure 11. (a) Typical AFM image recorded in tapping mode (loading force 10 nN) showing hillocks produced with 93 MeV ^{131}Xe^{23+} ($dE/dx = 14$ keV nm^{-1}); scan size 1000×1000 nm^2 (from [60]). (b) Height (right axis) and diameter (left axis) of surface hillocks on BaF$_2$ single crystals as a function of the energy loss of the ions [72]. The hillocks were produced with different ion beams. The size data of the hillocks was deduced from AFM images recorded in contact mode.
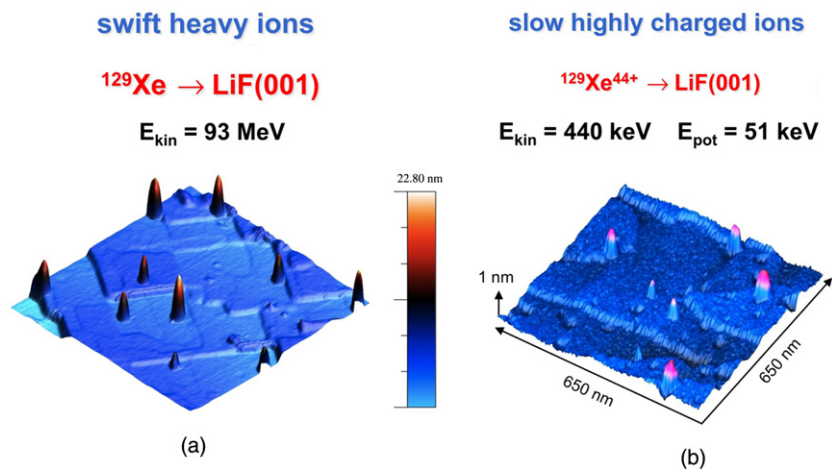

Figure 12. Hillocks created on a cleaved LiF single crystal surface after irradiation with (a) 93 MeV Xe ions (fluence 5×10^8 cm^{-2}; $dE/dx = 15$ keV nm^{-1}; image recorded under ambient conditions in tapping mode, scan size 1000×1000 nm^2; from [60]) and (b) 440 keV Xe^{44+} ions [73] (image obtained by contact AFM).

With contact mode AFM (loading force between 10 and 100 nN) in ambient conditions, hillocks from single impacts of 2.24 GeV Au ions ($dE/dx = 22$ keV nm^{-1}) are measured to have a height of ∼3 nm and a diameter of ∼55 nm [79]. Other experiments at lower stopping powers of $dE/dx = 15$ keV nm^{-1} found higher hillocks of up to ∼15 nm (see figure 12) [60]. Again, surface contaminations and measuring modes may influence absolute values considerably. The critical energy loss for hillock creation in LiF was determined to be 5 keV nm^{-1} [66]. Up to now, the composition of the hillocks, in particular the question of metallic Li clusters could not be identified but might be accessible with local probes such as Kelvin probe force microscopy. LiF thus could be an ideal system to compare details of defect creation induced by HCI and SHI, beyond the mere comparison of morphological features.

2.2. Oxides

2.2.1. Strontium titanate SrTiO₃.

Single crystals of strontium titanate SrTiO$_3$ were irradiated with slow highly charged [80, 81] and with high-energy Xe ions [82–84]. In both cases, inspection by AFM revealed nano-hillocks due to the impact of individual projectiles (figure 13). For irradiation under grazing incidence, each SHI produces a chain of equidistant nanodots separated by a few tens of nanometers [82, 83]. Similar to CaF$_2$, the formation of nano-hillocks on SrTiO$_3$ is linked to a critical electronic energy loss between 5.3 and 7.2 keV nm^{-1} [84] for SHI and to a less well known potential energy threshold above 15.4 keV for slow HCI [81].

Under normal incidence, the typical height of the hillocks on SrTiO$_3$ is $h \sim 4$ nm [82] for SHI of $dE/dx = 20$ keV nm^{-1} and $h \sim 6$ nm for ions of $dE/dx = 23$ keV nm^{-1} [67] (figure 13). Under ambient conditions, the hillock size slightly increases with time indicating possible environmental effects such as water adsorption. The influence of ambient conditions was excluded by performing the investigations in UHV and *in situ* (i.e. without breaking the vacuum) by means of dynamic AFM providing the highest resolution presently available. The observation of hillocks was confirmed and no signs of crater-like features could be detected. Preliminary studies of
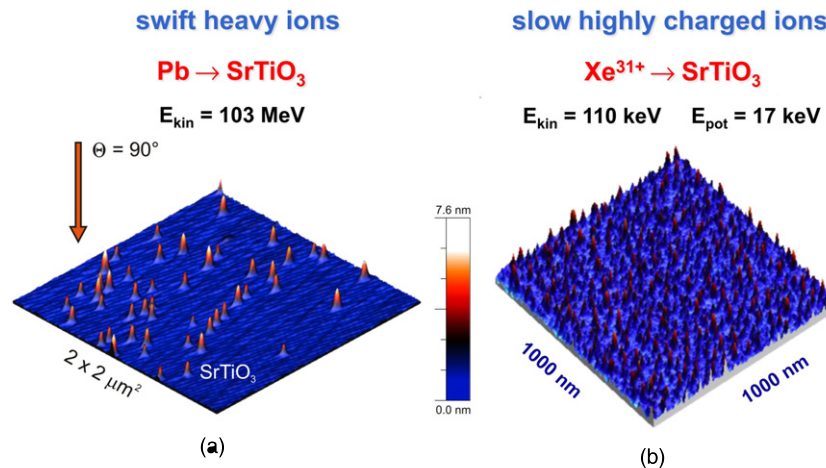
Figure 13. AFM images of SrTiO$_3$(100) surface irradiated with (a) 103 MeV ^{207}Pb ions (dE/dx = 23 keV nm^{-1}), imaged *in situ* in contact mode (loading force 0.2 nN) [86] and (b) 110 keV Xe^{31+} ions [81].
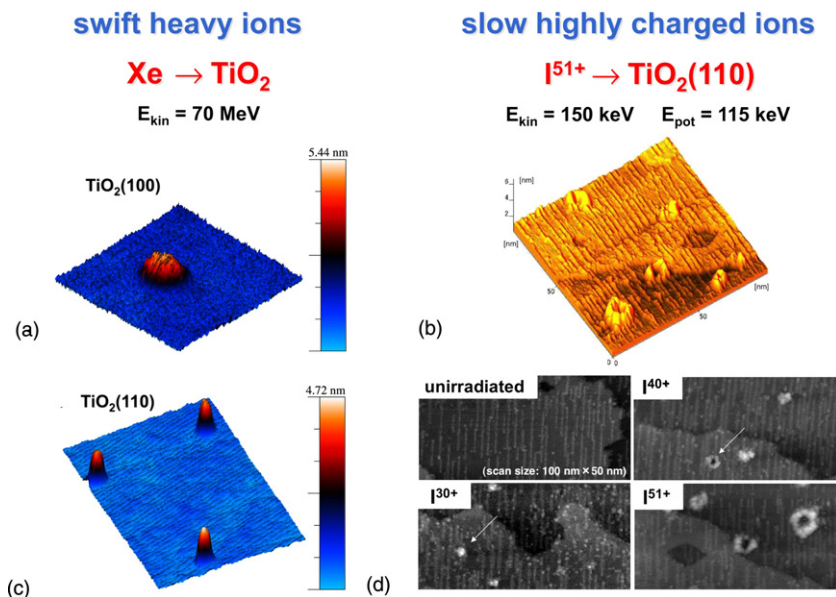

Figure 14. AFM images from (a) SHI induced hillocks on TiO$_2$(100) after irradiation with 0.5 MeV/amu ^{129}Xe ions [60] imaged under ambient conditions in tapping mode, frame size 190 × 140 nm^2 and (b) on TiO$_2$(110) imaged *in situ* in contact mode (loading force 0.2 nN), frame size 75 × 75 nm^2 [60]. (c) STM image of nano-sized craters formed on TiO$_2$(110) by impact of 150 keV I^{51+} ions [87] and (d) highly charged iodine ions of various charge states [87]. (c) and (d) have been reproduced with permission from [87]. Copyright 2008 American Physical Society.

photoluminescence properties in Duisburg–Essen indicated differences between the defect structure of HCI and SHI induced hillocks but details could not yet been specified [85].

2.2.2. Titanium dioxide TiO$_2$. Single crystals of TiO$_2$(110) surface were bombarded with highly charged I ions of 150 keV fixed kinetic energy, and a wide range of charge states from q = 25–51 [87]. Although TiO$_2$ is an oxide, high resolution images can be produced by scanning tunneling microscopy (STM) into empty surface states. Observations by the Tokyo EBIT group revealed nanometer-sized hillocks for low and intermediate charge states ($q < 40$) and caldera-like structures, i.e. craters with a rim, for ions of higher charge

states [87] (figure 14). The size of the observed structures strongly increases with q.

Crater-like structures were also reported after SHI irradiation of crystalline [88] as well as amorphous TiO$_2$ [89, 90]. Craters in crystalline TiO$_2$ were only achieved with 40 MeV I^{9+} (dE/dx = 13 keV nm^{-1}) but neither with 46 MeV I^{10+} (dE/dx = 14 keV nm^{-1}) nor with 1 GeV Ta projectiles (dE/dx = 35 keV nm^{-1}). The craters disappeared under different imaging conditions indicating that the ion impact zone is characterized by changed adsorption properties rather than being true topological features. In the case of amorphous TiO$_2$, the craters were not seen directly after the irradiation with 100 MeV Au ions (dE/dx = 23 keV nm^{-1}) but only after rapid thermal annealing. After the irradiation
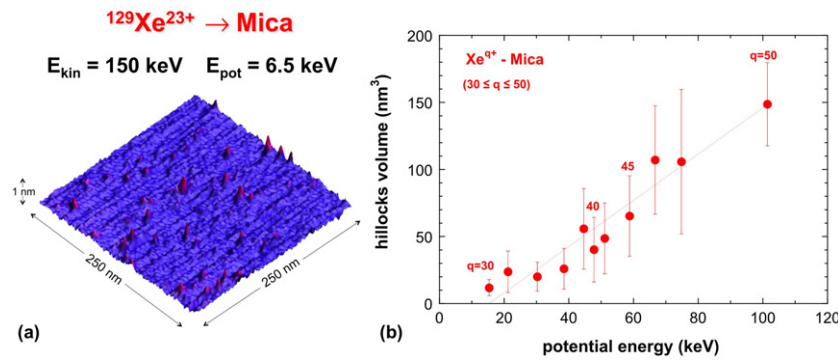
Figure 15. (a) Topographic contact mode AFM image (250 nm × 250 nm) of mica surface irradiated with 150 keV Xe^{23+} ions showing hillock-like nanostructures protruding from the surface as a result of individual ion impacts (figure reproduced with permission from [97]; copyright 2010 Elsevier). (b) Mean hillock volume as a function of potential energy on mica after irradiation with Xe^{q+} ions of charge $30 < q < 50$. Data taken from [93, 95].

with 150 MeV Cl ions ($dE/dx = 5.3$ keV nm^{-1}), hillocks of 5–7 nm height and $\sim$20 nm diameter were observed [91]. The hillocks were susceptible to chemical etching.

The irradiation of $TiO_2(110)$ as well as $TiO_2(100)$ samples with 0.5 MeV/amu Pb ions [67] and 0.7 MeV/amu Xe ions [60] of stopping power $S_e = 21$ keV nm^{-1} produces hillocks with a very similar height distribution as on $SrTiO_3$ [67]. The investigations were again in part performed under ultra-high vacuum conditions directly after the irradiation and can thus be compared to the *in situ* experiment of Tona *et al* [87]. The energy density deposited by SHI of stopping power $S_e = 21$ keV nm^{-1} is roughly comparable to the energy density of a highly charged I^{40+} assuming that the energy is spread within a sphere of 1.5 nm radius (see section 3.2). Figure 14(a) shows AFM images of TiO_2 surfaces recorded in contact mode under UHV conditions using a very sharp tip. There is no indication of a caldera-like structure as observed under HCI exposure. According to the images reported in [84] (figure 14(d)) only one of the impacts from I^{40+} ions exhibits a clear crater-like structure (marked with an arrow). The inner rim of the crater has a diameter of $\sim$1 nm, while the diameter of the outer rim is 6 nm. While the larger crater and rim structures produced by I^{51+} have a realistic chance to be detected, smaller features such as produced by I^{40+} impacts could go unnoticed in AFM imaging. To obtain similar structures with SHI (assuming that indeed the same structures are created) would, however, require much higher stopping powers of $S_e = 60$ keV nm^{-1}, which is out of reach for monatomic projectiles.

2.2.3. Muscovite mica. The mineral muscovite mica ($KAl_3Si_3O_{10}(OH)_2$) is an insulating, layered crystalline silicate which easily cleaves between two adjacent $SiO_4(001)$ lattice planes providing smooth and atomically flat surfaces. It was among the first materials to be studied with respect to ion induced surface modifications. Using AFM in air, topographic images of mica irradiated with various slow HCI (7q kV Kr^{35+}, Xe^{44+}, U^{70+} and Th^{74+}) were first reported by the Livermore group revealing the formation of what they called blister-like defects protruding from the surface [92–94]. From the area density of the observed blisters and the total number

of ions used they concluded that each hillock is the result of a single ion impact. The volume of the blisters was found to be proportional to the charge state and roughly proportional to the potential energy of the ions used [94] (figure 15). No structures could be identified in the AFM images for impacts of singly charged Xe^+ of similar kinetic energy (300 keV), not even when applying fluences ten times larger than for the HCI case [93]. Experiments with HCI were later repeated by the Kansas State University—NIST Gaithersburg collaboration [95, 96] using Xe^{q+} ions of charge states $25 \leq q \leq 50$ at fixed kinetic energy of 0.75 keV/amu. These authors observed circular hillocks, whose volume increased linearly with the potential energy of the projectile ions [95], but showed no pronounced dependence on the ions' kinetic energy [96]. For projectile ions of charge below $q = 30$ no surface structures were identified.

More recently, hillock formation was investigated for even lower potential energies by using slow Ar^{q+} ions (charge state $q = 12$, 16) and Xe^{q+} ($q = 23$, 27) ions in a kinetic energy range of 150–216 keV. Surprisingly, AFM images recorded in contact mode revealed hillock-like nanostructures on samples irradiated with Xe ions well below the charge state threshold reported earlier [97] (figure 15). Subsequent tapping mode AFM images showed that these structures are not topographic protrusions but rather nanofeatures of modified frictional behavior. This assumption was concluded from the fact that the signal of the detected structures depended on the scan condition and from the absence of these nanostructures in tapping mode images. In mica, the observed surface modifications obviously originate from frictional forces manifesting in height measurement artifacts. Furthermore the generated defects were not stable but could be erased by repeated AFM scans in contact mode [97].

Also for the irradiation with SHI, mica was one of the first systems to investigate ion impacts systematically by AFM. After the irradiation with Kr ions of stopping powers of up to 10.9 keV nm^{-1}. Thibaudau *et al* reported 'hollows' of 0.5 nm in depth and diameter of up to $\sim$6 nm [98]. The threshold for the formation of surface tracks characterized by changes in the AFM contrast is around 5 keV nm^{-1} [99–101]. Depressions measured in contact mode were correctly attributed to areas
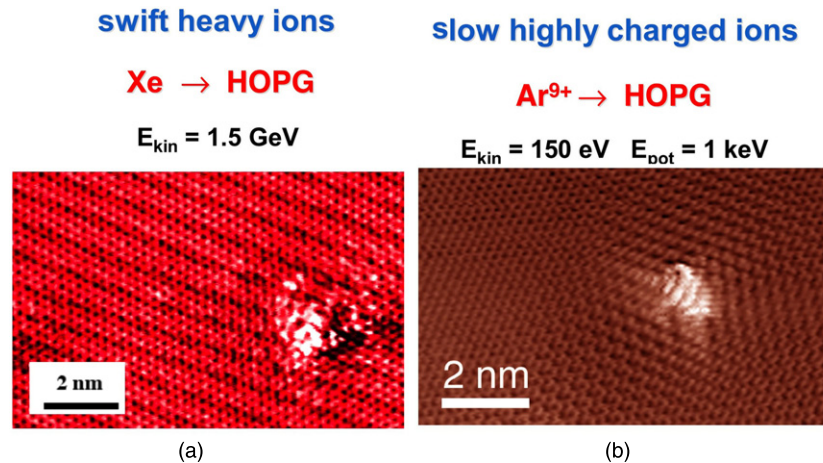
Figure 16. Individual ion impacts on HOPG surfaces studied by STM. The irradiations were performed with (a) 11.4 MeV amu^{-1} ^{136}Xe projectiles of $dE/dx = 15$ keV nm^{-1} [104, 107] and (b) 150 eV Ar^{9+} ions, potential energy $\sim$1 keV. Figures reproduced with permission from [104] and [107]. Copyright 2001 IOP Publishing and 2001 American Physical Society, respectively.

of higher friction and lower hardness, i.e. the tracks at the surface are characterized by changed elastic properties and not by topographic features. The track diameters, if measured by contact AFM, depend slightly on the loading force between the tip and the sample surface [37]. In later investigations it was shown that the depressions appear as protrusions with a height of $h \sim 0.5$ nm if imaged in tapping mode [102]. Obviously, the size depends on the imaging conditions.

Lang *et al* reported chemical etching of tracks in dark mica (phlogopite) produced with SHI of $dE/dx = 2.4$–10.4 keV nm^{-1} [103]. The geometry of the etch pits on the sample surface changed from a triangular to a hexagonal shape when increasing the energy loss between 5.7 and 8.8 keV nm^{-1}. The effect is ascribed to the transition from a discontinuous to continuous damage morphology along the tracks. It would be interesting to see if a similar transition could be observed by varying the charge state in a corresponding HCI experiment.

2.3. Highly oriented pyrolytic graphite HOPG

Among the few conducting materials susceptible to ion-beam induced damage, HOPG has been subject to a multitude of studies using slow HCI as well as SHI. HOPG is a layered material, consisting of parallel lattice planes with hexagonal ordering of the carbon atoms. The crystal can easily be cleaved because neighboring planes are connected by weak van der Waals forces. Within the planes the electric and thermal conductivity is high while perpendicular to the planes it is poor. HOPG can be imaged by STM in air with atomic resolution, defects and disorder of the crystal structure are thus easily detectable on a subnanometer scale.

The TU Wien group [104] studied surfaces exposed to ultra-slow (150 eV) singly and multiply charged Ar ions (charge state up to 9+) *in situ*, i.e. without breaking the UHV between irradiation and STM measurements. In all cases, the STM images showed hillock-like defects protruding from the atomically flat surface (figure 16(b)). Their area

density is in good agreement with the applied ion fluence, implying that every single ion impact causes one protrusion. A $\sqrt{3} \times \sqrt{3}$ R 30° surface reconstruction, characteristic for interstitial defects in HOPG, was observed in the vicinity of most defects (see figure 16(b)) [104–106]. The measured size of the hillocks (mean diameter and height) increases with projectile charge state [104].

An increase of hillock size on HOPG with the charge state of the impinging Ar^{q+} ($q \leq 8$) ions was also reported by Mochiji *et al* [108]. Since the protrusions were only visible in STM but not in AFM images, these authors concluded that the defects are of electronic rather than topographic nature.

Using Raman and tunneling spectroscopy Meguro *et al* [109] showed that the impact of single Ar^{q+} ions of $q \leq 8$ and subsequent treatment of the ion-irradiated spot by electron injection (either from the STM tip or by laser irradiation) induces a local transition from sp^2 to sp^3 hybridization in HOPG, resulting in the formation of nanoscale diamond-like structures (nano-diamonds) at the impact region.

The irradiation of HOPG was extended to higher charge states using Xe^{q+} projectiles ($q = 23, 44$ [110], $q \leq 46$ [111, 112]). The results of all STM measurements are summarized in figure 17, showing the hillock diameter as a function of the projectiles' potential energy. It is important to note, that the kinetic energy of the different experiments shown in figure 17 varied over a range of 1–200 keV but as demonstrated by Nakamura *et al* the kinetic energy of the ions has no significant influence on the hillock diameter and height [111]. Also, the hillock diameters as observed with AFM were nearly equal, the heights were slightly smaller than those observed with STM [111].

The size of the hillocks increases as a function of the potential energy, but their formation does not seem to require a minimum potential energy, because the impact sites are even observed for slow singly charged ions. Above a potential energy of $\sim$2 keV the hillock size versus potential energy correlation becomes much steeper (figure 17) which is probably an indication that the mechanism for hillock formation changes above this value.
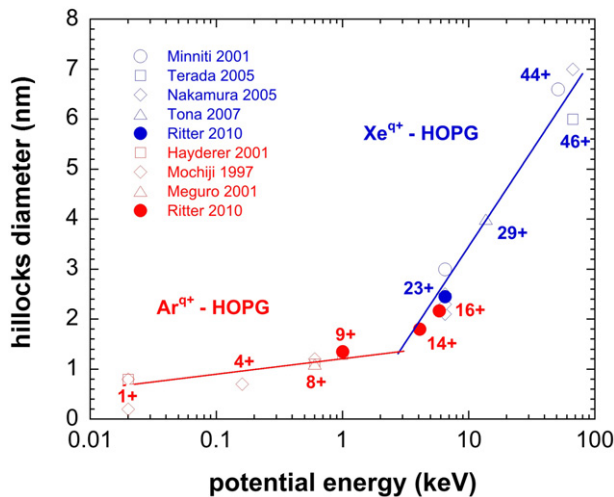
Figure 17. Hillock diameter as a function of potential energy for various HCI irradiations of HOPG observed by STM. Data taken from [104, 108–114].

In most studies, the damage of the ion impact site was ascribed to an enhancement of the local density of states caused by interstitial and vacancy defects rather than to a modification of the surface topography. To our knowledge, AFM imaging was only successful in one case where 138 keV Xe^{46+} ions were used [112]. Quite recently, we managed to image nanostructures by AFM for all combinations of charge states (Ar^{q+}, $q = 9$–16 and Xe^{q+}, $q = 13$–30) and kinetic energies (150–480 keV), if the AFM is operated in lateral force mode [114]. For these ions, the impact sites can therefore be interpreted as regions of enhanced friction while there is still no unambiguous indication for topographic protrusions. Employing a wedge calibration method for AFM cantilevers [115], we have quantitatively determined the microscopic friction force coefficient at the ion impact sites and its dependence on the ion charge state. First results indicate a clear size increase with higher charge states.

STM investigations of HOPG irradiated with swift heavy ions report very similar nanostructures (figure 16(a)) [107]. As in the case of HCI, the ion impact sites are significantly smaller than hillocks observed in other materials. The formation of ion tracks requires a threshold of $dE/dx = 7.3 \pm 1.5$ keV nm^{-1}. At this energy loss the damage is probably not continuous because the number of observed tracks is systematically smaller than the applied ion fluence. 100% efficiency (i.e. each ion produces a nanostructure) requires an energy loss above 18 keV nm^{-1} [107]. For extremely high fluences, craters have been reported [116] but they cannot be attributed to individual hits and sputtering effects have to be considered.

Beam induced changes of the crystalline structure emanating from the STM images were confirmed by Raman spectroscopy [117]. Furthermore, nano-diamonds were observed on the surface of SHI-exposed HOPG samples [118]. This is interesting because of the similarity with nano-diamonds created by the irradiation with HCI [119, 120]. If the sp^2 bonds of the graphite layers were changed

to sp^3 bonds, the local density of states and the surface contact potential would be affected as well as the tribological properties. For SHI, at least two studies observed ion tracks by AFM [121, 122]. However, the question of whether the ion induced features are truly topological in nature is difficult to answer, because STM as well as AFM record both topological and morphological changes. Unfortunately, true atomic resolution AFM imaging of HOPG in UHV environment is not feasible at room temperature [123].

2.4. Polymethyl methacrylate PMMA

Several polymers have been investigated with respect to surface modifications due to ion irradiation. However, numerous studies have been devoted to high fluence experiments which are not considered in this review. Most detailed data exists for polymethyl methacrylate (PMMA), probably because it is a common photoresist in the semiconductor industry. Patterning processes of silicon wafers use a few tens of nanometer thick PMMA film spin-coated on the Si surface. The wafer is then irradiated with a high fluence ($\sim 10^{13}$ cm^{-2}) of typically singly charged argon ions of moderate kinetic energies in the 10 keV regime. In beam-exposed areas of the PMMA, resist can be developed.

First investigations of HCI induced defects on PMMA were performed in the late 1990s by Gillaspy *et al* [124]. The treatment of the irradiated samples in isopropanol showed that the impacts of individual Xe^{44+} projectiles are converted into little craters while the unirradiated surface remained intact. Quite recently, more systematic studies were possible with highly charged Xe^{q+} ions ($q = 20$–50). Impact energies on the sample surface ranged from 0.35 to 4.0 keV/amu [125, 126]. Intermittent contact mode AFM investigations revealed that each individual ion creates a nano-sized crater (figure 18) [125]. The pit volume increases with the potential energy of the incoming ion, while increasing the kinetic energy of the beam seems to produce deeper and narrower pits, with the total volume remaining approximately the same [126].

In the case of PMMA exposed to SHI, craters were observed even with light ions such as oxygen, sulfur, bromium and iodine. Under grazing incidence, the diameter and depth of the craters are larger than under normal incidence and a raised tail extending along the direction of incidence appears behind each crater [128–130]. Papaleo *et al* [127] demonstrated that 3 MeV/amu Au^{q+} ions of various (non-equilibrium) charge states ($q = 30, 35, 40, 45$ and 51) can be used to tune the surface structures (figure 18) because the crater volume strongly increases with the deposited energy density. Additionally, the relaxation behavior of the ion impact zones near the glass transition temperature was studied in detail. The thermal response of the crater and rim are different probably due to different damage characteristics [131].

2.5. Other targets

2.5.1. Silicon Si. Using STM with atomic resolution Tona *et al* [132–134] recently observed radiation effects on
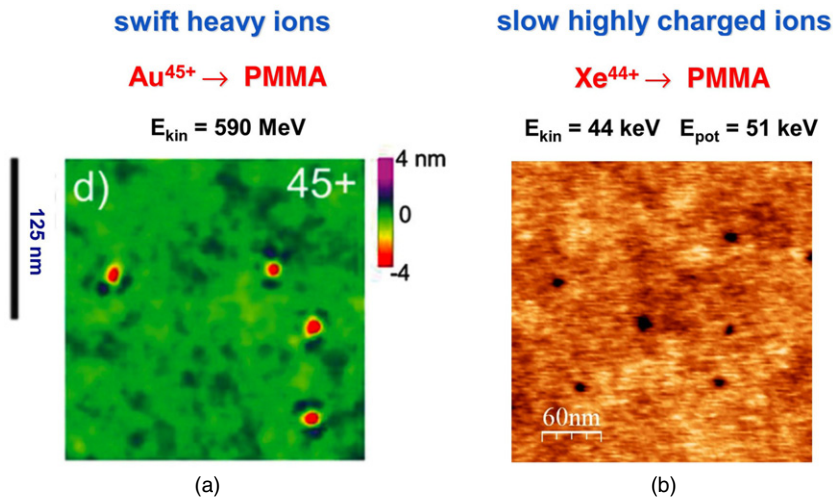
Figure 18. Craters produced by irradiating PMMA with (a) 3 MeV/amu ^{197}Au^{45+} ions [127] and (b) 44 keV ^{129}Xe^{44+} ions of 51 keV potential energy [125]. (a) has been reproduced with permission from [127]. Copyright 2008 American Physical Society.

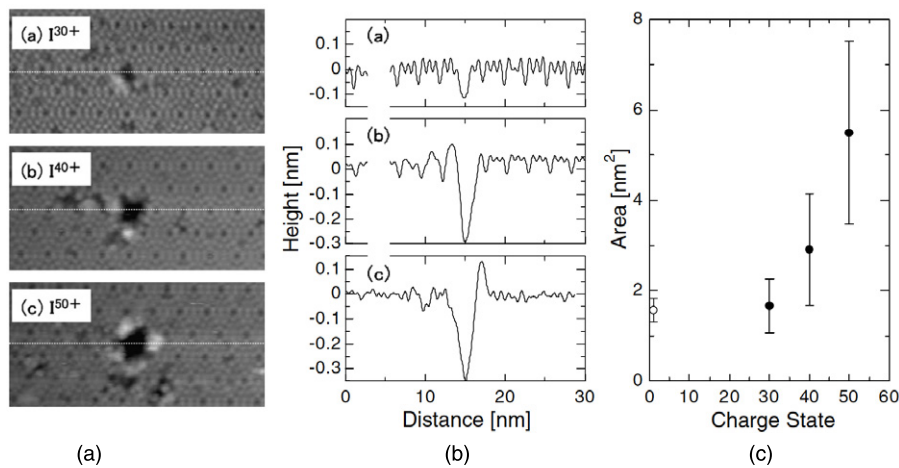**Figure 19.** (A) STM images of Si(111)-(7 $\times$ 7) irradiated with I^{q+}-ions of q = 30, 40, and 50. (B) Depth profiles obtained along the dashed lines in the corresponding STM images of (A). (C) Open area of the crater as a function of the charge q of the incident ion. Error bars represent the standard deviation of the measurements. Figures reproduced with permission from [132]. Copyright 2007 Elsevier.

Si(111)-7 $\times$ 7 after irradiation with slow HCI from the Tokyo EBIT. The Si surfaces were prepared *in situ* and bombarded with I^{q+} projectiles of charge state q = 30, 40 and 50 (impact energy 3 keV $\times$ q). STM images recorded without breaking the UHV revealed crater-like structures of typical diameters between 1.5 and 3 nm (see figure 19). In the atomically resolved STM images, the craters show brighter sites on the edges around the missing topmost layers. Depth profiles of the craters yielded depth values of at least 0.35 nm for I^{50+} impacts. The crater size becomes rapidly larger with increasing potential energy of the projectiles [132]. First indications of a potential energy threshold at around q = 30 have to be confirmed by a more systematic variation of the HCI charge state.

Crystalline silicon is one of the materials that does not form permanent tracks if monatomic projectiles are used. There have been several experiments to search for volume defects but according to the present status only 30–40 MeV C$_{60}$ projectiles providing a stopping power of more than

37 keV nm^{-1} yield track formation [135, 136]. According to the thermal spike model (see section 3.2) this is attributed to the fact that the energy deposited by monatomic projectiles is not high enough to reach the melting temperature of silicon (see also [137]). Even irradiation experiments of a single crystal Si(111)-7 $\times$ 7 surface with 0.92 MeV/amu Xe ions (dE/dx = 12 keV nm^{-1}) under glancing incidence which should in principle enhance the defect creation, showed no sign of defect creation by electronic stopping effects [138].

At present not much data exist on HCI irradiation of semiconductors which exhibit tracks when exposed to SHI such as, for example, Ge/GeO$_x$ [139], GaAs [140] or InP [141]. All these materials are usually terminated by dangling bonds. Due to their high reactivity, it is difficult to perform surface studies under ambient conditions and a big effort is required in preparing contamination free surfaces. Future systematic studies of semiconducting materials under controlled conditions are needed to clarify whether surface

damage by HCI is indeed comparable to SHI induced modifications.

2.5.2. Partially investigated targets. Nanometer-sized structures produced by individual HCI impacts were reported even on the high-conductivity surface of a gold single crystal [142]. After the irradiation of a Au(111) surface with Xe^{25+} and Xe^{44+} ions (impact energy 8 keV $\times q$), the STM examination was performed *in situ*. The potential energy seems less significant in forming features on gold than on low-free-electron density targets. The NIST group concludes that the primary formation mechanisms of the features they observe on Au(111) are probably not driven by potential energy but rather by the kinetic energy (nuclear stopping) [142]. Trying to repeat these experiments, the TU Wien group irradiated a Au(111) single crystal target with 440 keV Xe^{44+} ions [73], but was not able to detect any permanent surface modifications as a result of HCI irradiations. This might, however, be due to insufficient smoothness of the Au(111) sample (too high surface roughness) and/or the method of inspection (contact AFM in air) used.

To our knowledge no irradiation experiments with SHI have been performed on Au single crystal surfaces. Free-electron metals generally show no signs of SHI induced permanent modifications (e.g. [143, 144]) and tracks in crystalline metals have so far only been found in Bi, Zr and Ti [43, 143]. The insensitivity to irradiation damage has been attributed to the high electronic thermal conductivity of metals.

Several other target surfaces like Al_2O_3 [106], SiO_2 [105, 106] and DLC (diamond-like carbon) [73] have so far been explored. However, all these experiments were either not systematic enough (e.g. no variation of projectile charge state), inconclusive (insufficient surface preparation, the rough surface conditions preventing an unambiguous nanostructure identification) or not well reproducible. They will therefore be excluded from the discussion below.

3. Discussion of mechanisms

The experimental results for the different materials exposed to slow HCI and SHI reviewed above can be summarized as follows:

- The impact of individual slow highly charged or swift heavy ions may produce surface nanostructures of similar size. i.e. up to several tens of nanometers in diameter and a few nanometers in height or depth.
- For both types of ion beams, these nanostructures are observed mainly on insulators such as alkali and alkaline earth halides (KBr, LiF, CaF_2, BaF_2), oxides ($SrTiO_3$, TiO_2, mica) and polymers (PMMA) but also on HOPG (poor electrical conductivity perpendicular to basal planes). Nanostructures in isotropic metals of high electrical conductivity (Au) and pure semiconductors (Si) have been identified so far only for HCI.

- The nanostructures appear either as hillocks (CaF_2, LiF, mica, TiO_2, $SrTiO_3$, HOPG), craters- (sometimes also called pits) (KBr, Si, PMMA) or caldera-like structures (TiO_2, Au). The topography of the ion impact is probably determined by the amount of energy pumped into the topmost layers of the sample. Depending on the property of a given material, surface sputtering or bulk relaxation processes may be of crucial importance. Influences of ambient conditions and specific tip–probe interaction processes of scanning probe microscopy (STM or AFM) cannot be ruled out completely.
- In all materials investigated so far (HOPG, mica, CaF_2, BaF_2, PMMA, Si), the size (i.e. volume, diameter and height/depth) of the nanostructures generated by slow HCI depend strongly on their potential energy and is nearly independent of the kinetic energy, whereas the size of SHI impacts is ruled by the electronic stopping power.
- Similar to track formation in bulk material, SHI induced surface nanostructures require a well-defined threshold in electronic stopping power. In the case of HCI, a critical potential energy is needed as investigated in detail for CaF_2, but also evidenced for other targets such as KBr, $SrTiO_3$, mica and PMMA. In some materials (HOPG, Si) even slow singly charged ions produce defects visible by means of STM, i.e. the damage process is apparently not directly linked to a threshold. Nonetheless, the steep size increase of the nanostructures above a critical potential energy is probably an indirect indication for the existence of a threshold.

3.1. Energy deposition during interaction of slow HCI and SHI with solid surfaces

The striking similarity of nanostructures produced by HCI and SHI together with the observation of an energy threshold for both types of ion beams strongly suggests analog mechanisms of how the solid responds to the deposited energy. The following section elaborates common and different performances of slow HCI and SHI.

The slowing down process of singly charged or neutral atoms of keV/amu kinetic energy is dominated by elastic collisions with target atoms (nuclear stopping, figure 1(a)). Provided sufficient energy is transferred from the projectile, target atoms are directly displaced from their lattice site (figure 20(a)), otherwise they are vibrationally excited producing phonons. Defect creation via elastic collisions occurs in all solids, independent of the material class. Follow-up processes such as recombination and aggregation of defects are rather well understood.

In contrast, damage creation by SHI is more complex. Ions of high kinetic energy interact not directly with the atoms but with the electrons of the target inducing ionization and electronic excitation processes (electronic stopping, figure 1(a)). In particular MeV–GeV heavy ions transfer a huge amount of energy along their trajectory reaching up to several tens of keV per nanometer for high-mass target materials. The ion trajectory can be regarded as quasi-straight line because of the disparity of the mass of the ion and
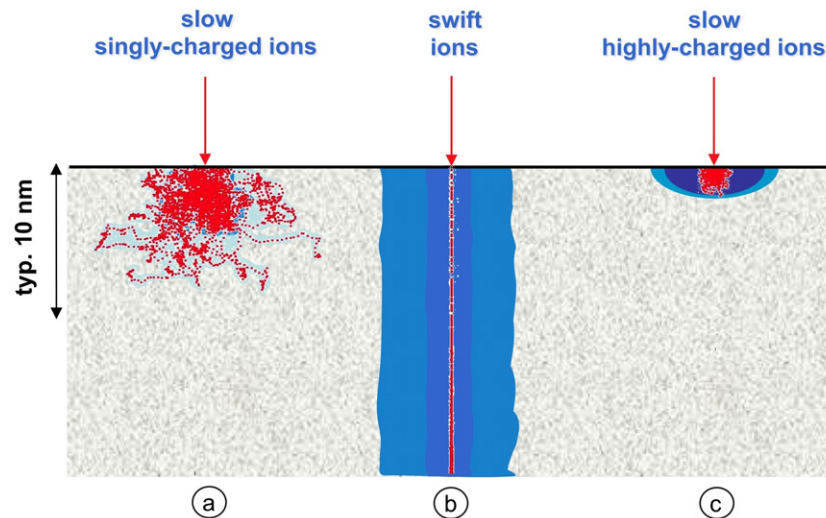
Figure 20. Scheme of energy deposition when ion projectiles interact with solids: (a) slow singly or low charged ions of keV–MeV kinetic energy: small range, energy loss dominated by elastic collisions (nuclear stopping), (b) swift ions of MeV–GeV kinetic energy, large range, energy loss dominated by electronic excitations, and (c) very slow highly charged ions, large potential energy (keV), very low (eV–keV) kinetic energy, very limited range. The trajectories of recoils are indicated in 'red'; electron induced electronic excitations of the solid are marked in 'blue' (adapted from [146]).

electron as collision partners. Following primary ionization, a cascade of secondary electrons develops and spreads radially, producing a cylindrical region of extremely high ionization density in particular close to the ion path (figure 20(b)) [6, 145]. The extension of the electron cascade is determined by fast electrons produced either in the primary ion–electron collisions or by inner-shell ionization processes. The energy initially deposited at the target electrons spreads and with some time delay is gradually transferred to the lattice atoms. Energy dissipation in the electron and atom subsystems occurs on quite different time scales. Atomic motion finally may destroy or modify the lattice structure of the solid.

Slow highly charged ions transfer their potential energy via a series of Auger processes and the consecutive emission of more or less energetic electrons into a shallow region close to the impact zone (figures 20(c) and 21) [1, 20]. Although the starting point is fundamentally different, the final outcome is very similar to the case of swift ions, namely a strong electronic excitation within a few nanometers around the ion impact site. Also the time scales of the different stages are approximately the same (figure 22). The close similarity in the energy deposition zone probably explains why surface nanostructures of SHI and HCI are so much alike.

3.2. Inelastic thermal spike concept

3.2.1. Swift heavy ions. The arguments presented above are a strong indication that for slow HCI and SHI the mechanisms by which the electronic excitation of the surface is transferred to the lattice atoms and finally leads to nanostructure formation are closely related or even identical [8, 13]. Before briefly discussing the main theoretical approaches so far available for SHI, let us recapitulate the different processes and relevant time scales (see e.g. [43]) (figure 21).

SHI pass through the target surface within attoseconds and ionize the atoms in a cylindrical region of a few nm

in diameter. Charge neutralization, e.g. by Auger transitions, occurs on time scales of a few fs [147]. The electrons are still energetically excited and thermalize by electron–electron scattering within several hundred fs at the most [148] which is comparable with time scales found in experiments with fs laser excitation [149]. Up to this stage the contribution of the lattice atoms is insignificant because the cross sections of electron–atom scattering are low due to the large energy and mass mismatch. Possible mechanisms for how the energy initially deposited in the electron system is finally converted into atomic motion and defect creation are described by different models. The time-span of the formation of tracks or surface nanostructures is enormous ranging from 10^{-18} s up to 100 ps and above. An all-encompassing theoretical description including the scenario of the electrons as well as atoms is not available. Instead, largely phenomenological descriptions are available handling crucial stages of the above-mentioned scenario by different concepts.

- Under intensive electronic excitations, the crystal structure may be directly affected by the strong modification of the inter-atomic forces. From pump–probe experiments, it is known that in such a situation atoms can rapidly acquire sufficient kinetic energy to induce melting [149–151]. This process has been described for several semiconductors and is called ultra-fast or non-thermal melting because it occurs within sub-picoseconds and is much faster than the time required to transfer the electronic energy into the lattice and yield thermal motion.

- The Coulomb explosion model assumes that the ionized atoms gain kinetic energy under the influence of their mutual repulsion [4, 12, 152]. The atomic movement depends on the screening time given by returning electrons, being slow in insulators and rapid in metals. The mechanism was originally proposed by Fleischer *et al* [4], when tracks were observed exclusively in insulating
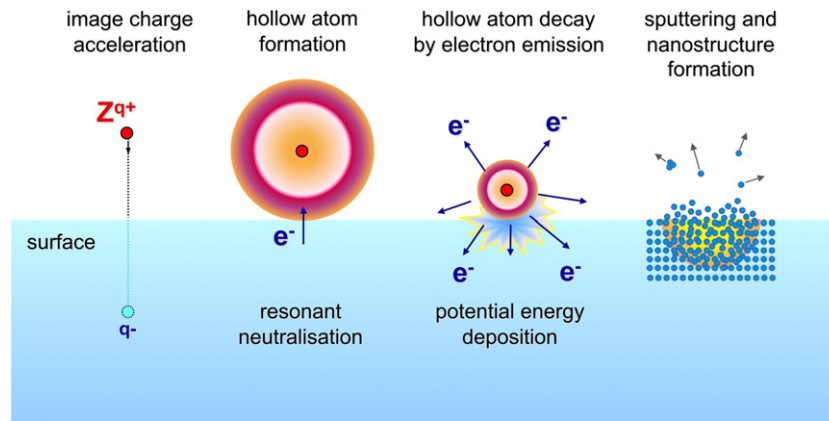
Figure 21. Current understanding of the interaction scenario when slow HCI impact a solid surface [1, 35, 146]. From left to right: the HCI approaches the surface by acquiring image charge energy gain. Close to the surface, the ion picks up an electron from the target and forms a hollow atom. The hollow atom decays at and below the surface by electron- and x-ray emission. The potential energy of the HCI is deposited in a small volume close to the surface producing ionization and electronic excitation processes, eventually leading to potential sputtering and nanostructure formation.
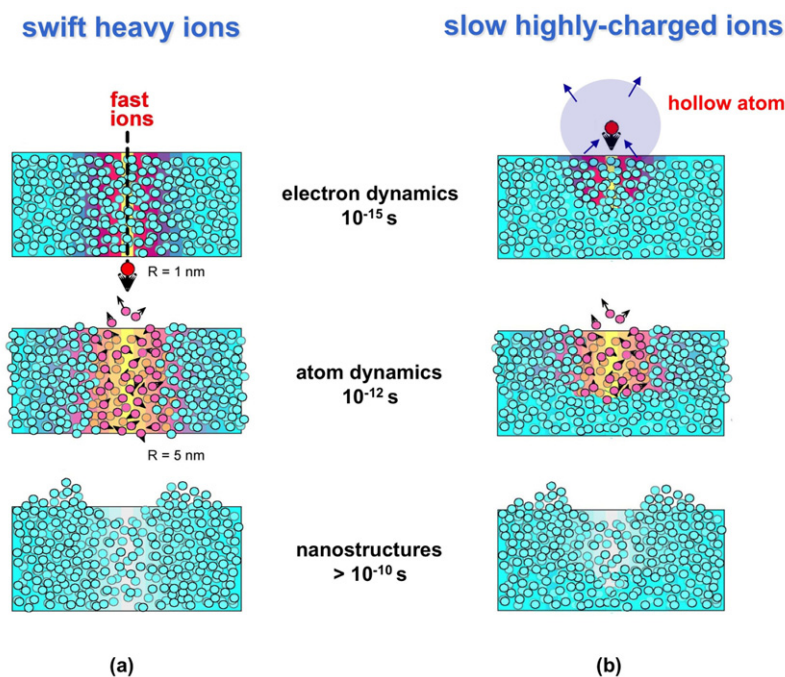

Figure 22. Time evolution of the interaction of (a) a swift heavy ion and (b) a slow highly charged ion with a solid surface. In both cases the initial interaction excites the electronic system on a femtosecond time scale, while atomic motion and creation of disorder happen on a picosecond time scale. Upon rapid thermal cooling, the disorder in the atomic system is quenched. On the surface, craters or hillocks of nanometric dimensions are formed. For SHI the damage extends deep into the bulk forming a cylindrical track: (a) has been reproduced with permission from [147]. Copyright 2004 Elsevier; (b) was adapted from (a) with permission from the artist (Schiwietz).

materials. Later tracks were also evidenced in some metals, and several attempts were undertaken to calculate the repulsive forces and estimate whether the strength and lifetime were large enough to induce atomic motion [12, 153]. However, to this day, there is no Coulomb explosion description available that is sufficiently developed to correctly reproduce experimental observations or provide useful predictions.

- In thermal spike approaches, track formation is linked to local lattice heating [8, 154]. 10^{-14}–10^{-13} s after the initial electron excitation, energy is transferred to the lattice via electron–phonon coupling. The lattice is heated until the electronic system and the atoms reach thermal equilibrium (typically within some picoseconds). Subsequently, the hot lattice dissipates the energy to the surrounding cold matrix material for a period of up to 100 ps. If the thermal spike reaches temperatures above melting and if the following cooling rate is high enough, the molten phase is frozen in. The remaining disordered cylinder is commonly called an ion track.
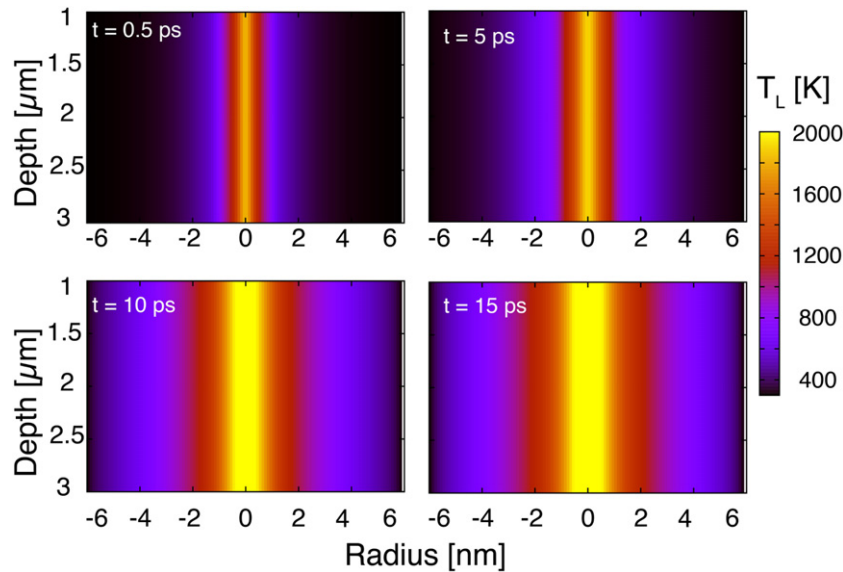
Figure 23. Thermal spike calculation for irradiation of crystalline SiO_2 (T_{melt} = 1400 K, latent heat of fusion 142 kJ kg^{-1}) with 11.4 MeV/amu Ca ions (dE/dx = 2.6 keV nm^{-1}) showing temperature profiles along the ion trajectory at different times after ion impact. After ≈15 ps the maximum spatial spread of the temperature profile is reached. Figure provided by Osmani (unpublished).

The most elaborated thermal spike concept is based on the two-temperature model (TTM) [155–157]. Because the electronic excitation and atomic motion occur on different time scales, the model treats the thermal diffusion equations of both subsystems as quasi-independent, yet coupled via electron–phonon coupling as an energy exchange term. In a recent extension by Medvedev *et al* [148], the very first steps of the excitation are elaborated in more detail by including ionization, charge neutralization and electron thermalization processes. For a specific material/projectile combination all relevant quantities such as the electron number density and their energy density are calculated as a function of space and time via a Monte Carlo (MC) approach. The calculations provide the time, when the electronic system is still excited but thermalized. First calculations [158] show that after ~100 fs the electronic system can typically be described via a thermodynamic temperature. After this time, energy transfer processes can be followed in space and time by solving a set of coupled classical heat transport equations. Relevant input parameters such as electron and hole distributions, electron–phonon coupling strength, and electron diffusivity are deduced from the MC calculations [159]. Combining the MC approach with the TTM basically yields a parameter-free code for lattice temperature profiles (see figure 23), which are in good agreement with experimental data [160]. This extension partly clarifies open questions on the applicability of the equilibrium heat transport equation, at least for the electron subsystem [161].

The resulting lattice temperature depends on the efficiency of the coupling between the electronic system and the lattice as well as on energy localization mechanisms of a given solid and can reach up to thousands of degrees (hence the name thermal spike). The specific time and radial profile of the temperature depends on the electronic and thermal properties of the solids and on the energy density deposited by the projectile. For metals and amorphisable insulators, track formation is linked to the criteria of local melting, i.e. a cylindrical region around the ion trajectory contains sufficient energy to be transformed into the molten phase. During subsequent cooling, this liquid is rapidly quenched, freezing a highly disordered track region. Track formation requires that the electron system does not dissipate the energy too quickly but provides a sufficient amount to be transferred to the atoms. Many track recording materials are also characterized by an efficient energy localization mechanism e.g. by self-trapping of excitons [43].

Although far from being complete, the standard two-temperature model gives for many materials surprisingly accurate descriptions of the evolution of experimental track radii with electronic stopping as well as the energy loss threshold for track formation [8]. Direct confirmation of the different track formation stages suffers from the lack of access to transient parameters such as electron energy and ionization density. Most studies are based on post-mortem analysis and do not provide data on such short time scales. In this regard, extended MD simulations would be extremely helpful although challenging due to the electronic energy deposition and the rather large interaction volumes required. Recent MD simulations of atomic motion during the heating and cooling phase give good agreement with experimental findings [160, 162]. The approach is encouraging and should certainly be extended to more material/projectile combinations, in particular because it will eventually provide more information on the defect nature. Simulations could also be of interest to separate surface and bulk effects which are difficult to access experimentally. Track phenomena and surface sputtering with SHI have been studied so far only for a few materials [163, 164]. From the binding situation, the damaged area is expected to be larger on the surface than in the bulk and the thresholds should be lower, however the special situation has
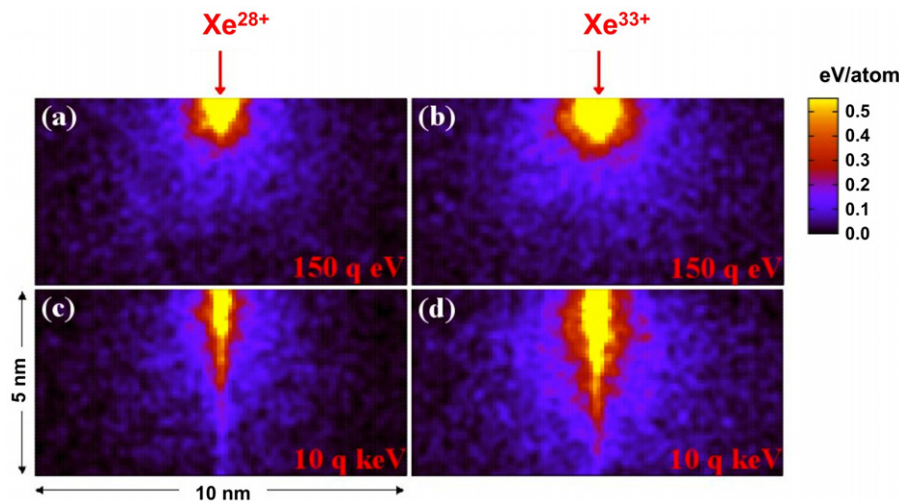
Figure 24. Model calculations of the energy density deposited by slow highly charged Xe ions in a CaF$_2$ crystal: (a), (c) Xe^{28+} and (b), (d) Xe^{33+}, for two different impact energies, (a), (b) 150q eV and (c), (d) 10q keV [15]. Melting requires 0.55 eV/atom.

not been investigated as the theoretical models are not yet refined enough to make precise predictions with respect to experimentally accessible parameters such as hillock or crater size.

3.2.2. Slow highly charged ions. The close similarity of HCI and SHI induced surface structures together with the existence of 'energy thresholds' suggests that the inelastic thermal spike model [13] may also be appropriate in the case of slow HCI [14]. In the group of Burgdörfer and Lemell a microscopic model [15, 63, 165] has been developed and was first applied to explain the results observed for HCI impacts on CaF$_2$. In this model the process is divided into three stages, which take place on different time scales (figure 22): energy deposition from the projectile to the electronic system of the target, energy diffusion from the electronic system into the lattice, and atomic motion. The different processes are modeled sequentially using the results of the preceding step as input for the subsequent step.

- In the first step, the potential energy of the projectile is deposited in the electronic system of the target and converted into kinetic energy of primary emitted electrons. Highly charged ions approaching solid surfaces undergo a large number of neutralization and deexcitation processes (figure 21) which are well described within the classical-over-barrier model developed for metal surfaces [166–168] and later extended for insulator targets [169]. Electrons from the target are transferred into highly excited states of the projectile, which may decay by collisional, radiative and Auger processes. This leaves unbalanced holes in the target surface; they store part of the potential energy carried into the collision and weaken the structure of the target. Projectiles reach the surface far from the ground state as the time spent close to the surface is not sufficient for complete relaxation. At this stage, electrons are captured into moderately excited states by either resonant charge transfer from the valence band or Auger neutralization

processes followed by an Auger deexcitation sequence. Along this sequence, electrons with low to intermediate energies up to a few hundred electron volts are emitted. If inner-shell holes are to be filled, electrons with keV kinetic energies are released. The potential energy of the HCI is deposited along the first few nanometers below the target surface (figure 20). The kinetic energy of the projectile determines the depth within which the neutralization is completed (1 nm for 150q eV and 4 nm for 10q keV projectiles; see figure 24). It is much smaller than the total range of the ion in the solid [2, 3]. According to model calculations, a single HCI with $q = 40$ creates, for example, about 250 unbalanced holes in CaF$_2$ [170, 171] which significantly can affect the crystal structure of the target.

- The second step of the model calculation involves a Monte Carlo type electron transport simulation. Elastic and inelastic scattering processes are taken into account and the trajectories of secondary electrons are followed. Finally, phonons are excited in collisions of electrons with lattice atoms and the lattice temperature increases. Melting requires a high-energy density (> 0.55 eV/atom for CaF$_2$), which is available close to the ion trajectory where mainly low-energy electrons contribute. High-energy electrons distribute their energy over a much larger volume because of their larger inelastic and elastic mean free paths [63]. Surprisingly and contrary to simple expectations, the decisive difference between ions of charge state below or above the threshold are not faster Auger electrons but the larger number of slow electrons emitted along the deexcitation sequence when the additional inner-shell holes are filled. Figure 24 shows the calculated energy density along the path of highly charged Xe projectiles of different potential and kinetic energy. Close to the trajectory the energy per atom is high enough to reach melting (bright yellow region). The shape of the molten volume strongly depends on the velocity of the projectile, being almost hemispherical for slow projectiles
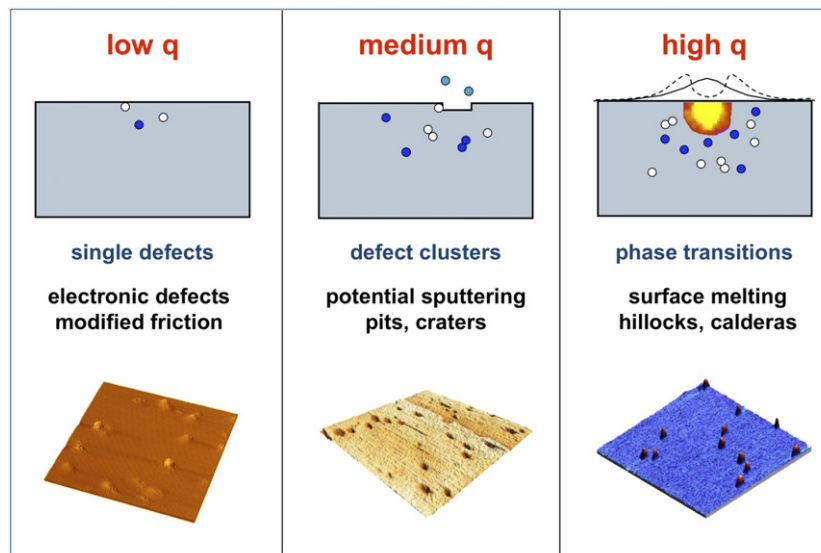
Figure 25. Scenario of defect creation for slow ions of different charge state q (compare with text).

(figures 24(a) and (b)) and having the shape of a candle flame for fast projectiles. The shape is thus quite different compared to the SHI case but the radial dimensions are similar (see figure 23). The diameter of the heated volume shrinks if either the HCI velocity is increased or the potential energy is reduced (smaller initial charge states). Hillock formation is experimentally observed for ions displayed in figures 24(a), (b), and (d), while for Xe^{28+} of $10q$ keV (figure 24(c)) the diameter of the molten region is reduced to about one lattice constant, which is obviously too small to produce surface hillocks.

- The last step of the model calculations involves lattice restructuring processes and takes place on a picosecond time scale (figure 22). MD simulations are most appropriate to quantify the melting and cooling process in detail. Preliminary simulations of the Burgdörfer group show good agreement with experimental threshold values [165] successfully linking the potential energy thresholds observed for CaF_2 (figures 6(b) and 7) to nano-melting at the impacted surface [62, 63]. The simulations also evidence that the process is almost independent of the kinetic energy but is governed by the potential energy deposited in the first few target layers. This explains why the size of the observed surface features in first order does not change with the kinetic energy of the impinging ions.

So far this microscopic model has not been extended to other target materials. The threshold in potential energy is expected to depend on material properties such as the free-electron density and electron transport parameters (elastic and inelastic mean free path). To demonstrate its general applicability more systematic investigations for various target materials have to be performed. As shown in section 2 in some materials nano-sized surface modifications are already visible (or become visible after chemical etching) for HCI projectiles in lower charge states, i.e. before nano-melting

occurs. It should be clarified whether these observations fit into a more general picture.

Based on the present experimental findings, we suggest to describe nanostructure formation with slow HCI using the following scenario: for singly charged ions or ions of low charge state (figure 25, left) individual defects are created at or below the surface, depth details depend on the potential and kinetic energy of the projectile. If these defects remain below the surface, anneal or are extremely small (e.g. single vacancies) they may not be detected by means of tapping or non-contact AFM. Future investigations should test whether they can be observed as electronic defects by high resolution STM [106] or due to modified friction by lateral force AFM [114].

With increasing charge state (figure 25, center), the potential sputtering yield strongly increases [1, 21–25], sometimes assisted by the kinetic energy of the projectiles [172]. The density of defects (excitons, color centers etc) is large enough leading to defect clusters. Depending on their mobility, defects may diffuse to the surface and form (monatomic) pits as observed in the case of KBr. Kinetically induced defects created in the collision cascade amplify the trapping of the electron–hole pairs created by the potential energy [55] and therefore enhance defect formation (the boundary region between 'pits' and 'no-pits' in figure 3 therefore has a negative slope).

At still higher projectile charges (figure 25, right), heating of the lattice atoms by primary and secondary electrons from the deexcitation of the HCI surpasses the melting threshold of the solid. Heat and pressure deforms the surface and after cooling down a hillock- or caldera-like structure remains at the surface. With increasing kinetic energy, the region where the potential energy of the HCI is deposited shifts slightly deeper into the target [63]. The kinetic energy dependence of the boundary region between 'hillock' and 'no-hillock' in figure 3 is therefore rather weak.

The boundaries between scenarios A, B and C depend on material parameters. In some materials other phase changes may occur such as a transitions from the crystalline to the amorphous state. Figure 25 should thus be considered as a simplified scenario.

4. Open problems

Based on the materials studied so far, it is evident that surface nanostructures induced by SHI and HCI exhibit very analog features including similar size parameters and the requirement of an energy density threshold. However, there are also numerous subtle differences, e.g. SHI produce in general hillocks (craters were observed only in highly radiolytic polymers), whereas HCI-exposed materials exhibit a larger variety showing hillocks (CaF_2, BaF_2, LiF, $SrTiO_3$), craters (Si, TiO_2), and pits (KBr). Moreover, HCI produce craters in Si while no tracks or surface structures were observed with SHI unless C_{60} cluster beams were used.

The primary excitation processes of SHI and HCI are rather different, e.g. for SHI the energy of primary electrons is high producing a much larger number of secondary ionization events than in the case of HCI. Moreover, the larger number of these high-energy electrons, traveling ballistically away from their point of origin, can reduce the deposited energy density in the case of SHI impacts.

The significance of the SHI–HCI analogy is at present difficult to judge because none of the many experiments have been performed under absolutely identical conditions. Up to now, there exists no systematic study for a given material using both ion beams and applying exactly the same analytical methods. An important issue concerns surface contaminations, which may influence quantitative results quite significantly and need to be investigated more systematically, e.g. by performing experiments without breaking the ultra-high vacuum conditions.

The comparison of existing HCI and SHI data gives important indications of common basic processes but it also leaves many open questions to be answered, e.g.

- What is the composition and structure of the hillock material (e.g. for CaF_2 targets, hillocks may consist of fluorine depleted Ca clusters or metallic colloids).
- Is the material modification for a given material identical for SHI and HCI? Are slow HCI able to induce amorphization like SHI?
- If hillock formation by HCI is due to nano-melting, a second threshold should exist at still higher potential energy corresponding to sublimation (first indications for such a second threshold was observed for CaF_2 [62]).
- Is thermal melting required for hillock formation or is the process of non-thermal melting more realistic as reported for fs laser irradiated solids [151].
- Why do we see pits or craters in some cases and hillocks in others? Is the scenario presented in figure 25 realistic?
- What is the specific role of surface contaminations and environmental (e.g. humidity) conditions?

- Which other materials are susceptible to surface nanostructuring by slow HCI?

The general understanding of surface modifications by HCI will improve if additional materials can be investigated, in particular those for which track data produced with SHI are available, such as diamond-like carbon (DLC), $Y_3Fe_5O_{12}$, Al_2O_3, SiO_2 or $LiNbO_3$. The results will allow us to test whether the phenomena can be described by one of the suggested track models (e.g. the inelastic thermal spike model or Coulomb Explosion). In lamellar material with large anisotropies (e.g. HOPG, mica or two-dimensional graphene nanosheets), the energy of the electrons will preferentially be transported within the planes, imposing an additional challenge on modeling the anisotropy of the process. It also needs to be clarified whether surface nanostructures are formed in materials with high density of free electrons (e.g. metals). The efficient dissipation of the HCIs potential energy may prohibit the formation of nanostructures or at least enlarge the threshold energies required for their production.

Finally, we like to conclude this contribution with our vision that slow highly charged ions may become a gentle but efficient tool for surface nanostructuring [173]. Future activities should explore the possibilities for HCI lithography and surface patterning [124], or novel products based on tunnel barriers with HCI-tailored resistance areas [174]. Using HCI beams as tools for surface modifications is rather new, but given the striking analogies, this field may profit from the knowledge and expertise already available for swift heavy ions.

Acknowledgments

References

[1] Aumayr F and Winter H P 2004 *Phil. Trans. R. Soc.* **362** 77
[2] Ziegler J F 2006 www.srim.org
[3] Ziegler J F, Biersack J P and Littmark U 1985 *The Stopping and Range of Ions in Matter* vol 1 (New York: Pergamon)
[4] Fleischer R L, Price P B and Walker R M 1965 *J. Appl. Phys.* **36** 3645
[5] Dammak H, Dunlop A, Lesueur D, Brunelle A, Della-Negra S and Le Beyec Y 1995 *Phys. Rev. Lett.* **74** 1135
[6] Schiewietz G, Luderer E, Xiao G and Grande P L 2001 *Nucl. Instrum. Methods Phys. Res.* B **175** 1
[7] Chadderton L T 2003 *Radiat. Meas.* **36** 13

[8] Toulemonde M, Assmann W, Dufour C, Meftah A, Studer F and Trautmann C 2007 *Mater. Fys. Med. Dan. Vid. Selsk.* **52** 263

[9] Spohr R 1990 *Ion Tracks and Microtechnology, Principles and Applications* (Braunschweig: Vieweg)

[10] Toulemonde M, Trautmann C, Balanzat E, Hjort K and Weidinger A 2004 *Nucl. Instrum. Methods* B **216** 1

[11] Gnaser H 1999 *Low-Energy Ion Irradiation of Solid Surfaces* vol 146 (Berlin: Springer)

[12] Lesueur D and Dunlop A 1993 *Radiat. Eff. Defects Solids* **126** 163

[13] Toulemonde M, Dufour C and Paumier E 1992 *Phys. Rev.* B **46** 14362

[14] Aumayr F, El-Said A S and Meissl W 2008 *Nucl. Instrum. Methods* B **266** 2729

[15] El-Said A S *et al* 2008 *Phys. Rev. Lett.* **100** 237601

[16] Facsko S, Meissl W, Heller R, Wilhelm R, El-Said A S, Kowarik G, Ritter R and Aumayr F 2009 *J. Phys.: Conf. Ser.* **194** 012060

[17] Facsko S, Heller R, El-Said A S, Meissl W and Aumayr F 2009 *J. Phys.: Condens. Matter* **21** 224012

[18] Hagstrum H D 1954 *Phys. Rev.* **96** 325

[19] Hagstrum H D 1954 *Phys. Rev.* **96** 336

[20] Arnau A *et al* 1997 *Surf. Sci. Rep.* **27** 113

[21] Neidhart T, Pichler F, Aumayr F, Winter H P, Schmid M and Varga P 1995 *Phys. Rev. Lett.* **74** 5280

[22] Neidhart T, Pichler F, Aumayr F, Winter H P, Schmid M and Varga P 1995 *Nucl. Instrum. Methods Phys. Res.* B **98** 465

[23] Varga P, Neidhart T, Sporn M, Libiseller G, Schmid M, Aumayr F and Winter H P 1997 *Phys. Scr.* **T73** 307

[24] Sporn M, Libiseller G, Neidhart T, Schmid M, Aumayr F, Winter H P, Varga P, Grether M and Stolterfoht N 1997 *Phys. Rev. Lett.* **79** 945

[25] Hayderer G, Schmid M, Varga P, Winter H P, Aumayr F, Wirtz L, Lemell C, Burgdörfer J, Hagg L and Reinhold C O 1999 *Phys. Rev. Lett.* **83** 3948

[26] Kuroki K, Okabayashi N, Torii H, Komaki K and Yamazaki Y 2002 *Appl. Phys. Lett.* **81** 3561

[27] Okabayashi N, Komaki K and Yamazaki Y 2005 *Nucl. Instrum. Methods Phys. Res.* B **232** 244

[28] Hasselkamp D 1992 *Particle Induced Electron Emission II* ed G Höhler (Heidelberg: Springer) p 1

[29] Schou J 1988 *Scanning Microsc.* **2** 607

[30] Rösler M and Brauer W 1991 *Particle Induced Electron Emission I* ed G Höhler (Berlin: Springer)

[31] Toglhofer K, Aumayr F and Winter H P 1993 *Surf. Sci.* **281** 143

[32] Eder H, Aumayr F and Winter H P 1999 *Nucl. Instrum. Methods* B **154** 185

[33] Juaristi J I, Auth C, Winter H, Arnau A, Eder K, Semrad D, Aumayr F, Bauer P and Echenique P M 2000 *Phys. Rev. Lett.* **84** 2124

[34] Sigmund P 1993 *Fundamental Processes in Sputtering of Atoms and Molecules (SPUT 92)* vol 43 (Copenhagen: Mat. Fys. Medd.) p 2

[35] Winter H P and Aumayr F 1999 *J. Phys. B: At. Mol. Opt. Phys.* **32** R39

[36] Winter H P and Aumayr F 2002 *Eur. Phys. News* **33** 215

[37] Aumayr F and Winter H P 2007 *Springer Tr Mod Phys* vol 225, ed H P Winter and J Burgdörfer (Berlin: Springer) pp 79–112

[38] Neumann R 1999 *Nucl. Instrum. Methods Phys. Res.* B **151** 42

[39] Stoneham A M and Itoh N 2000 *Appl. Surf. Sci.* **168** 186

[40] Itoh N and Stoneham A M 2001 *Radiat. Eff. Defect Solids* **155** 277

[41] Schwartz K, Trautmann C and Neumann R 2003 *Nucl. Instrum. Methods Phys. Res.* B **209** 73

[42] Akcöltekin S, Akcöltekin E, Schleberger M and Lebius H 2009 *J. Vac. Sci. Technol.* B **27** 944

[43] Itoh N, Duffy D M, Khakshouri S and Stoneham A M 2009 *J. Phys.: Condens. Matter* **21** 474205

[44] Giessibl F J 2000 *Science* **289** 422

[45] Jung T, Mo Y W and Himpsel F J 1995 *Phys. Rev. Lett.* **74** 1641

[46] Mizes H A, Park S and Harrison W A 1987 *Phys. Rev.* B **36** 4491

[47] Khalfaoui N, Görlich M, Müller C, Schleberger M and Lebius H 2006 *Nucl. Instrum. Methods* B **245** 246

[48] Albrecht T R and Quate C F 1987 *J. Appl. Phys.* **62** 2599

[49] Barth C and Henry C 2003 *Phys. Rev. Lett.* **91** 196102

[50] Müller C, Voss K O, Lang M and Neumann R 2003 *Nucl. Instrum. Methods* B **212** 318

[51] Khalfaoui N, Rotaru C C, Bouffard S, Toulemonde M, Stoquert J P, Haas F, Trautmann C, Jensen J and Dunlop A 2005 *Nucl. Instrum. Methods* B **240** 819

[52] Nonnenmacher M, O'Boyle M and Wickramasinghe H K 1992 *Ultramicroscopy* **42–44** 268

[53] Sigmund P and Schinner A 2002 *Nucl. Instrum. Methods* B **195** 64

[54] Toulemonde M 2006 *Nucl. Instrum. Methods* B **250** 263

[55] Heller R, Facsko S, Wilhelm R A and Möller W 2008 *Phys. Rev. Lett.* **101** 096102

[56] Möller W, Eckstein W and Biersack J P 1988 *Comput. Phys. Commun.* **51** 355

[57] Möller W and Eckstein W 1984 *Nucl. Instrum. Methods* B **2** 814

[58] Balanzat E, Bouffard S, Cassimi A, Doorhyee E, Protin L, Grandin J P, Doualan J L and Margerie J 1994 *Nucl. Instrum. Methods* B **91** 134

[59] Kimura K and Imamura M 1978 *Phys. Lett.* A **67** 159

[60] Akcöltekin E 2007 *Diploma Thesis* Universität Duisburg–Essen unpublished

[61] El-Said A S, Meissl W, Simon M C, Lopez-Urrutia J R C, Gebeshuber I C, Lang M, Winter H, Ullrich J and Aumayr F 2007 *Nucl. Instrum. Methods* B **256** 346

[62] El-Said A S *et al* 2007 *Nucl. Instrum. Methods* B **258** 167

[63] Lemell C, El-Said A S, Meissl W, Gebeshuber I C, Trautmann C, Toulemonde M, Burgdörfer J and Aumayr F 2007 *Solid State Electron.* **51** 1398

[64] Jensen J, Dunlop A, Della-Negra S and Toulemonde M 1998 *Nucl. Instrum. Methods* **146** 412

[65] Roll T, Meier M, Akcöltekin S, Klusmann M, Lebius H and Schleberger M 2008 *Phys. Status Solidi* R **2** 209

[66] Müller C, Cranney M, El-Said A S, Ishikawa N, Iwase A, Lang M and Neumann R 2002 *Nucl. Instrum. Methods Phys. Res.* B **191** 246

[67] Akcöltekin S, Akcöltekin E, Roll T, Lebius H and Schleberger M 2009 *Nucl. Instrum. Methods* B **267** 1386

[68] Boccanfuso M, Benyagoub A, Schwartz K, Trautmann C and Toulemonde M 2002 *Nucl. Instrum. Methods* B **191** 301

[69] Davidson A T, Kozakiewicz A G, Comins J D, Derry T E, Schwartz K and Trautmann C 2002 *Radiat. Eff. Defect Solids* **157** 637

[70] El-Said A S, Heller R, Aumayr F and Facsko S 2010 *Phys. Rev.* B **82** 033403

[71] El-Said A S, Heller R and Facsko S 2011 *Nucl. Instrum. Methods Phys. Res.* B **269** 901

[72] El-Said A S, Cranney M, Ishikawa N, Iwase A, Neumann R, Schwartz K, Toulemonde M and Trautmann C 2004 *Nucl. Instrum. Methods Phys. Res.* B **218** 492

[73] El-Said A S, Meissl W, Simon M C, Crespo Lopez-Urrutia J R, Gebeshuber I C, Laimer J, Winter H P, Ullrich J and Aumayr F 2007 *Radiat. Eff. Defects Solids* **162** 467

[74] Young D A 1958 *Nature* **182** 375

[75] Young D A 2004 *Nucl. Instrum. Methods* B **225** 231

[76] Trautmann C, Schwartz K and Geiss O 1998 *J. Appl. Phys.* **83** 3560

[77] Kotomin E A, Kashcheyevs V, Kuzovkov V N, Schwartz K and Trautmann C 2001 *Phys. Rev. B* **64** 144108

[78] Trautmann C, Toulemonde M, Costantini J M, Grob J J and Schwartz K 2000 *Phys. Rev. B* **62** 13

[79] Müller A, Neumann R, Schwartz K and Trautmann C 1998 *Nucl. Instrum. Methods B* **146** 393

[80] Peters T, Haake C, Hopster J, Sokolovsky V, Wucher A and Schleberger M 2009 *Nucl. Instrum. Methods B* **267** 687

[81] El-Said A S, Wilhelm R A, Heller R, Facsko S, Trautmann C and Aumayr F 2011 *Nucl. Instrum. Methods Phys. Res. B* **269** 1234

[82] Akcöltekin E, Peters T, Meyer R, Duvenbeck A, Klusmann M, Monnet I, Lebius H and Schleberger M 2007 *Nature Nanotechnol.* **2** 290

[83] Akcöltekin E, Akcöltekin S, Osmani O, Duvenbeck A, Lebius H and Schleberger M 2008 *New J. Phys.* **10** 053007

[84] Karlusic M, Akcöltekin S, Osmani O, Monnet I, Lebius H, Jaksic M and Schleberger M 2010 *New J. Phys.* **12** 043009

[85] Peters T, Karlusic M, Ruth M and Schleberger M, unpublished results

[86] Akcöltekin S, Bukowska H, Peters T, Osmani O, Monnet I, Alzaher I, Ban d'Etat B, Lebius H and Schleberger M 2011 *Appl. Phys. Lett.* **98** 103103

[87] Tona M, Fujita Y, Yamada C and Ohtani S 2008 *Phys. Rev. B* **77** 155427

[88] Popok V N, Jensen J, Vuckovic S, Mackova A and Trautmann C 2009 *J. Phys. D: Appl. Phys.* **42** 205303

[89] Thakurdesai M, Sulania I, Narsale A M, Kanjilal D and Bhattacharyya V 2008 *J. Nanosci. Nanotechnol.* **8** 4387

[90] Thakurdesai M, Kanjilal D and Bhattacharyya V 2008 *Appl. Surf. Sci.* **254** 4695

[91] Awazu K, Wang X M, Fujimaki M, Komatsubara T, Ikeda T and Ohki Y 2006 *J. Appl. Phys.* **100** 044308

[92] Schneider D, Briere M A, Clark M W, McDonald J, Biersack J and Siekhaus W 1993 *Surf. Sci.* **294** 403

[93] Schneider D H, Briere M A, McDonald J and Biersack J 1993 *Radiat. Eff. Defects Solids* **127** 113

[94] Ruehlicke C, Briere M A and Schneider D H 1995 *Nucl. Instrum. Methods Phys. Res. B* **99** 528

[95] Parks D C, Stöckli M P, Bell E W, Ratliff L P, Schmieder R W, Serpa F G and Gillaspy J D 1998 *Nucl. Instrum. Methods Phys. Res. B* **134** 46

[96] Parks D C, Bastasz R, Schmieder R W and Stöckli M 1995 *J. Vac. Sci. Technol. B* **13** 941

[97] Ritter R, Kowarik G, Meissl W, El-Said A S, Maunoury L, Lebius H, Dufour C, Toulemonde M and Aumayr F 2010 *Vacuum* **84** 1062

[98] Thibaudau F, Cousty J, Balanzat E and Bouffard S 1991 *Phys. Rev. Lett.* **67** 1582

[99] Chailley V, Dooryhee E, Bouffard S, Balanzat E and Levalois M 1994 *Nucl. Instrum. Methods B* **91** 162

[100] Bouffard S, Leroy C, Della-Negra S, Brunelle A and Costantini J M 2001 *Phil. Mag. A* **81** 2841

[101] Ackermann J, Müller A, Neumann R and Wang Y 1998 *Appl. Phys. A* **66** S1151

[102] Daya D D N B, Reimann C T, Hallen A, Sundqvist B U R and Hakansson P 1996 *Nucl. Instrum. Methods B* **111** 87

[103] Lang M, Glasmacher U A, Moine B, Neumann R and Wagner G A 2004 *Nucl. Instrum. Methods B* **218** 466

[104] Hayderer G, Cernusca S, Schmid M, Varga P, Winter H and Aumayr F 2001 *Phys. Scr.* **T92** 156

[105] Gebeshuber I C, Cernusca S, Aumayr F and Winter H P 2003 *Nucl. Instrum. Methods* **205** 751

[106] Gebeshuber I C, Cernusca S, Aumayr F and Winter H P 2003 *Int. J. Mass Spectrom.* **229** 27

[107] Liu J, Neumann R, Trautmann C and Müller C 2001 *Phys. Rev. B* **64** 184115

[108] Mochiji K, Yamamoto S, Shimizu H, Ohtani S, Seguchi T and Kobayashi N 1997 *J. Appl. Phys.* **82** 6037

[109] Meguro T, Hida A, Koguchi Y, Miyamoto S, Yamamoto Y, Takai H, Maeda K and Aoyagi Y 2003 *Nucl. Instrum. Methods Phys. Res. B* **209** 170

[110] Minniti R, Ratliff L P and Gillaspy J D 2001 *Phys. Scr.* **T92** 22

[111] Nakamura N, Terada M, Nakai Y, Kanai Y, Ohtani S, Komaki K and Yamazaki Y 2005 *Nucl. Instrum. Methods Phys. Res. B* **232** 261

[112] Terada M, Nakamura N, Nakai Y, Kanai Y, Ohtani S, Komaki K and Yamazaki Y 2005 *Nucl. Instrum. Methods Phys. Res. B* **235** 452

[113] Tona M *et al* 2007 *J. Phys.: Conf. Ser.* **58** 331

[114] Ritter R, Kowarik G, Meissl W, Suss L, Maunoury L, Lebius H, Dufour C, Toulemonde M and Aumayr F 2010 *Nucl. Instrum. Methods B* **268** 2897

[115] Varenberg M, Etsion I and Halperin G 2003 *Rev. Sci. Instrum.* **74** 3362

[116] Tripathi A, Khan S A, Kumar M, Baranwal V, Krishna R and Pandey A C 2006 *Nucl. Instrum. Methods B* **244** 225

[117] Liu J *et al* 2003 *Nucl. Instrum. Methods Phys. Res. B* **212** 303

[118] Dunlop A, Jaskierowicz G, Ossi P M and Della-Negra S 2007 *Phys. Rev. B* **76** 155403

[119] Koguchi Y, Meguro T, Hida A, Takai H, Maeda K, Yamamoto Y and Aoyagi Y 2003 *Nucl. Instrum. Methods B* **206** 202

[120] Meguro T, Hida A, Koguchi Y, Miyamoto S, Yamamoto Y, Takai H, Maeda K and Aoyagi Y 2003 *Nucl. Instrum. Methods B* **209** 170

[121] Bouffard S, Cousty J, Pennec Y and Thibaudau F 1993 *Radiat. Eff. Defects Solids* **126** 225

[122] Akcöltekin S, El Kharrazi M, Köhler B, Lorke A and Schleberger M 2009 *Nanotechnology* **20** 155601

[123] Schwarz A, Schwarz U D, Langkat S, Hölscher H, Allers W and Wiesendanger R 2002 *Appl. Surf. Sci.* **188** 245

[124] Gillaspy J D, Parks D C and Ratliff L P 1998 *J. Vac. Sci. Technol. B* **16** 3294

[125] Ginzel R *et al* 2010 *Nucl. Instrum. Methods B* **268** 2972

[126] Ritter R, Kowarik G and Aumayr F, unpublished results

[127] Papaleo R M, Silva M R, Leal R, Grande P L, Roth M, Schattat B and Schiwietz G 2008 *Phys. Rev. Lett.* **101** 167601

[128] Kopniczky J, Reimann C T, Hallen A, Sundqvist B U R, Tengvall P and Erlandsson R 1994 *Phys. Rev. B* **49** 625

[129] Daya D D N B *et al* 1995 *Nucl. Instrum. Methods B* **106** 38

[130] Papaleo R M, Leal R, Trautmann C and Bringa E M 2003 *Nucl. Instrum. Methods B* **206** 7

[131] Papaleo R M, Hasenkamp W, Barbosa L G and Leal R 2006 *Nucl. Instrum. Methods B* **242** 190

[132] Tona M, Watanabe H, Takahashi S, Nakamura N, Yoshiyasu N, Sakurai M, Terui T, Mashiko S, Yamada C and Ohtani S 2007 *Surf. Sci.* **601** 723

[133] Tona M, Watanabe H, Takahashi S, Nakamura N, Yoshiyasu N, Sakurai M, Terui T, Mashiko S, Yamada C and Ohtani S 2007 *Nucl. Instrum. Methods B* **256** 543

[134] Tona M, Watanabe H, Takahashi S, Nakamura N, Yoshiyasu N, Sakurai M, Yamada C and Ohtani S 2007 *Nucl. Instrum. Methods B* **258** 163

[135] Dunlop A, Jaskierowicz G and Della-Negra S 1998 *Nucl. Instrum. Methods B* **146** 302

[136] Canut B, Bonardi N, Ramos S M M and Della-Negra S 1998 *Nucl. Instrum. Methods Phys. Res. B* **146** 296

[137] Chettah A, Kucal H, Wang Z G, Kac M, Meftah A and Toulemonde M 2009 *Nucl. Instrum. Methods B* **267** 2719

[138] Osmani O, Alzaher I, Peters T, d'Etat B B, Cassimi A, Lebius H, Monnet I, Medvedev N, Rethfeld B and Schleberger M 2011 *Nucl. Instrum. Methods Phys. Res.* B in revision

[139] Batra Y, Kabiraj D, Kumar S and Kanjilal D 2009 *Surf. Coat. Technol.* **203** 2415

[140] Schnohr C S, Kluth P, Giulian R, Llewellyn D J, Byrne A P, Cookson D J and Ridgway M C 2010 *Phys. Rev. B* **81** 075201

[141] Kamarou A, Wesch W, Wendler E, Undisz A and Rettenmayr M 2008 *Phys. Rev. B* **78** 054111

[142] Pomeroy J M, Perrella A C, Grube H and Gillaspy J 2007 *Phys. Rev. B* **75** 241409(R)

[143] Trautmann C 2010 *Ion Beams in Nanoscience and Technology* (Berlin: Springer) p 369

[144] Mieskes H, Assmann W, Grüner F, Kucal H, Wang Z and Toulemonde M 2003 *Phys. Rev. B* **67** 155414

[145] Arnoldbik W M, Tomozeiu N and Habraken F H P M 2003 *Nucl. Instrum. Methods Phys. Res. B* **203** 151

[146] Aumayr F and Winter H P 2005 *Nucl. Instrum. Methods B* **233** 111

[147] Schiwietz G, Czerski K, Roth M, Staufenbiel F and Grande P L 2004 *Nucl. Instrum. Methods B* **226** 4

[148] Medvedev N A, Volkov A E, Rethfeld B and Shcheblanov N S 2010 *Nucl. Instrum. Methods B* **268** 2870

[149] Rethfeld B, Kaiser A, Vicanek M and Simon G 2002 *Phys. Rev. B* **65** 214303

[150] Saeta P, Wang J K, Siegal Y, Bloembergen N and Mazur E 1991 *Phys. Rev. Lett.* **67** 1023

[151] Rethfeld B, Sokolowski-Tinten K, von der Linde D and Anisimov S I 2002 *Phys. Rev. B* **65** 092103

[152] Yavlinskii Y N 2006 *Nucl. Instrum. Methods B* **245** 114

[153] Klaumünzer S, Hou M D and Schumacher G 1986 *Phys. Rev. Lett.* **57** 850

[154] Toulemonde M, Dufour C, Meftah A and Paumier E 2000 *Nucl. Instrum. Methods Phys. Res. B* **166/167** 903

[155] Kaganov M I, Lifshitz I M and Tanatarov L V 1957 *Sov. Phys. JETP—USSR* **4** 173

[156] Anisimov S I, Kapeliovich B L and Perelman T L 1974 *Sov. Phys. JETP—USSR* **39** 375

[157] Martynenko I V and Iavlinskii I N 1983 *Dokl. Akad. Nauk. Sssr+* **270** 88

[158] Osmani O, Medvedev N, Schleberger M and Rethfeld B 2011 *Phys. Rev. B* submitted

[159] Osmani O, Medvedev N, Schleberger M and Rethfeld B 2010 *Surf. Sci. Nanotechnol.* **8** 278

[160] Kluth P *et al* 2008 *Phys. Rev. Lett.* **101** 175503

[161] Klaumünzer S 2006 *Kong Dansk Vidensk* **52** 293

[162] Duffy D M, Itoh N, Rutherford A M and Stoneham A M 2008 *J. Phys.: Condens. Matter* **20** 082201

[163] Toulemonde M, Assmann W, Trautmann C and Gruner F 2002 *Phys. Rev. Lett.* **88** 057602

[164] Assmann W, Toulemonde M and Trautmann C 2007 *Top. Appl. Phys.* **110** 401

[165] Wachter G 2009 *Diploma Thesis* TU Wien—Vienna University of Technology unpublished

[166] Burgdörfer J, Lerner P and Meyer F W 1991 *Phys. Rev. A* **44** 5674

[167] Burgdörfer J 1993 *Fundamental Processes and Applications of Atoms and Ions* ed C D Lin (Singapore: World Scientific)

[168] Lemell C, Winter H P, Aumayr F, Burgdörfer J and Meyer F W 1996 *Phys. Rev. A* **53** 880

[169] Wirtz L, Reinhold C O, Lemell C and Burgdörfer J 2003 *Phys. Rev. A* **67** 12903

[170] Meissl W, Winklehner D, Aumayr F, Simon M C, Ginzel R, Crespo López-Urrutia J R, Ullrich J, Solleder B, Lemell C and Burgdörfer J 2008 *Surf. Sci. Nanotechnol.* **6** 54

[171] Aumayr F, Kurz H, Schneider D, Briere M A, Mcdonald J W, Cunningham C E and Winter H P 1993 *Phys. Rev. Lett.* **71** 1943

[172] Hayderer G *et al* 2001 *Phys. Rev. Lett.* **86** 3530

[173] Aumayr F and Winter H P 2003 *e-J. Surf. Sci. Nanotechnol.* **1** 171

[174] Pomeroy J M, Grube H, Perrella A C and Gillaspy J 2007 *Appl. Phys. Lett.* **91** 073506